# Space-based measurements of stratospheric mountain waves by CRISTA
# 1. Sensitivity, analysis method, and a case study

Peter Preusse,[1,2] Andreas Dörnbrack,[3] Stephen D. Eckermann,[4] Martin Riese,[1,2] Bernd Schaeler,[1] Julio T. Bacmeister,[5] Dave Broutman,[6] and Klaus U. Grossmann[1]

Received 29 March 2001; revised 27 August 2001; accepted 28 August 2001; published 25 September 2002.

[1] The Cryogenic Infrared Spectrometers and Telescopes for the Atmosphere (CRISTA) instrument measured stratospheric temperatures and trace species concentrations with high precision and spatial resolution during two missions. The measuring technique is infrared limb-sounding of optically thin emissions. In a general approach, we investigate the applicability of the technique to measure gravity waves (GWs) in the retrieved temperature data. It is shown that GWs with wavelengths of the order of 100–200 km horizontally can be detected. The results are applicable to any instrument using the same technique. We discuss additional constraints inherent to the CRISTA instrument. The vertical field of view and the influence of the sampling and retrieval imply that waves with vertical wavelengths ~3–5 km or larger can be retrieved. Global distributions of GW fluctuations were extracted from temperature data measured by CRISTA using Maximum Entropy Method (MEM) and Harmonic Analysis (HA), yielding height profiles of vertical wavelength and peak amplitude for fluctuations in each scanned profile. The method is discussed and compared to Fourier transform analyses and standard deviations. Analysis of data from the first mission reveals large GW amplitudes in the stratosphere over southernmost South America. These waves obey the dispersion relation for linear two-dimensional mountain waves (MWs). The horizontal structure on 6 November 1994 is compared to temperature fields calculated by the Pennsylvania State University (PSU)/National Center for Atmospheric Research (NCAR) mesoscale model (MM5). It is demonstrated that precise knowledge of the instrument's sensitivity is essential. Particularly good agreement is found at the southern tip of South America where the MM5 accurately reproduces the amplitudes and phases of a large-scale wave with 400 km horizontal wavelength. Targeted ray-tracing simulations allow us to interpret some of the observed wave features. A companion paper will discuss MWs on a global scale and estimates the fraction that MWs contribute to the total GW energy (Preusse et al., in preparation, 2002). *INDEX TERMS:* 3334 Meteorology and Atmospheric Dynamics: Middle atmosphere dynamics (0341, 0342); 3360 Meteorology and Atmospheric Dynamics: Remote sensing; 3384 Meteorology and Atmospheric Dynamics: Waves and tides

**Citation:** Preusse, P., A. Dörnbrack, S. D. Eckermann, M. Riese, B. Schaeler, J. T. Bacmeister, D. Broutman, and K. U. Grossmann, Space-based measurements of stratospheric mountain waves by CRISTA, 1. Sensitivity, analysis method, and a case study, *J. Geophys. Res.*, *107*(D23), 8178, doi:10.1029/2001JD000699, 2002.

## 1. Introduction

[2] Gravity waves (GWs) are important for the middle atmosphere dynamics and composition. Originating from lower altitudes, GWs propagate upwards into the stratosphere and mesosphere where they deposit momentum and energy when breaking. Therefore GWs strongly influence the global circulation and are thought to be a major cause of global-scale oscillations such as the Quasi Biennial Oscillation (QBO) [*Dunkerton*, 1997, and references therein] and the Semiannual Oscillation (SAO) [e.g., *Mayr et al.*, 1998].

[3] However, most current global circulation models are not able to explicitly resolve GWs because of the coarse spatial resolution of the models. Even models which can be run for case studies with sufficient resolution to resolve GWs have to parameterize GWs for long-term runs due to computing constraints. The importance of a good representation of GWs to obtain realistic global circulation, mean wind and temperature structures as well as QBO and SAO

[1]Department of Physics, Wuppertal University, Wuppertal, Germany.
[2]Now at ICG-I, Forschungszentrum Jülich, Jülich, Germany.
[3]Institut für Physik der Atmosphäre, Deutsches Zentrum für Luft und Raumfahrt (DLR), Oberpfaffenhofen, Germany.
[4]E. O. Hulburt Center for Space Research, Naval Research Laboratory, Washington, District of Columbia, USA.
[5]Goddard Earth Sciences and Technology Center (GEST), University of Maryland, Baltimore County (UMBC), Baltimore, Maryland, USA.
[6]Also at Computational Physics Inc., Springfield, Virginia, USA.


0148-0227/02/2001JD000699$09.00

patterns has been highlighted by many authors [e.g., *Boville*, 1995; *Manzini et al.*, 1997; *Manzini and McFarlane*, 1998; *McLandress*, 1998].

[4] A fundamental question in this context is what and where the major wave sources are. Waves excited by flow over mountains (mountain waves, MWs), have zero phase speeds relative to the ground (at least as long as the wind speed does not change strongly with time) in contrast to GWs from other sources such as convection. Because nonorographic GWs have different impacts on the synoptic-scale dynamics, they are commonly treated by different parameterization schemes [*Boville*, 1995; *Manzini and McFarlane*, 1998]. Thus there is interest in determining the sources of observed GWs and in estimating the fraction that orographic GWs contribute to the total GW flux entering the middle atmosphere on global scale [*Nastrom and Fritts*, 1992].

[5] Breaking GWs not only deposit momentum but also induce turbulence and thus enhance turbulent mixing in the atmosphere. This influences the chemical composition especially in the upper mesosphere where wave breaking is intense [*Garcia and Solomon*, 1985; *Summers et al.*, 1997].

[6] Furthermore GWs might play an important role in the ozone depletion in the Arctic winter and spring. While temperatures in the Arctic on global scales normally remain too warm to form polar stratospheric clouds (PSC) and thereby activate chlorine radicals, temperatures may drop locally below the frost point in the presence of strong MWs as observed in the lee of the Scandinavian mountains [*Dörnbrack et al.*, 1999]. Given the high number of mountain ridges at high latitudes in the northern hemisphere, such events should occur rather frequently and therefore be a significant source of PSCs on synoptic scales [*Carslaw et al.*, 1999a, 1999b; *Dörnbrack et al.*, 2001; *Dörnbrack and Leutbecher*, 2001].

[7] In recent decades most observational studies of GWs have used ground-based data from a limited number of locations [e.g., *Fritts*, 1984; *Tsuda et al.*, 1991; *Eckermann et al.*, 1995; *Allen and Vincent*, 1995]. Even large coordinated networks of ground-based and in situ measurements, such as the Planetary Scale Mesopause Observing System (PSMOS) and the Stratospheric Processes And their Role in Climate (SPARC) programs, still cannot provide true global coverage. Global coverage is now provided by a rapidly increasing number of GW studies from satellites. To date, GW signals have been analyzed on global scales using temperature data acquired by the Limb Infrared Monitor of the Stratosphere (LIMS) [*Fetzer*, 1990; *Fetzer and Gille*, 1994, 1996], 63 GHz limb radiances measured by the Microwave Limb Sounder (MLS) [*Wu and Waters*, 1996a, 1996b, 1997; *McLandress et al.*, 2000; *Jiang and Wu*, 2001], temperature data from the Cryogenic Infrared Spectrometers and Telescopes for the Atmosphere (CRISTA) [*Eckermann and Preusse*, 1999; *Preusse et al.*, 1999, 2000], and temperature retrievals from the meteorological program for the Global Positioning System (GPS/MET) [*Tsuda et al.*, 2000; *Nastrom et al.*, 2000]. In addition, in the upper mesosphere/lower thermosphere data from the Wind Imaging Interferometer (WINDII) were investigated for GWs [*Wang et al.*, 2000a, 2000b, 2001a, 2001b]. GWs have also been investigated in saturated radiances taken by the SPIRIT-3 radiometer on board the Midcourse Space Experiment (MSX) satellite for two case studies [*Dewan et al.*, 1998; *Picard et al.*, 1998].

[8] In case of the LIMS and the CRISTA instrument GW data are inferred from optically thin emission limb measurements. Other instruments using the same technique are the Cryogenic Limb Array Etalon Spectrometer (CLAES) [*Roche et al.*, 1993] and the SABER (Sounding of the Atmosphere using Broadband Emission Radiometry) instrument [*Mertens et al.*, 2001]. In addition, the upcoming mission of the High-Resolution Dynamics Limb Sounder (HIRDLS) on board the Earth Observing System Chem (EOS-Chem) satellite will provide similar global measurements at a rate of ~8000 profiles a day with global coverage [*Barnett et al.*, 1998]. The high spatial resolution of these data ought to make this instrument very well suited for GW studies.

[9] This paper provides a detailed assessment of GW fluctuations (and MWs in particular) observed in temperature data acquired by CRISTA infrared limb scan observations. Many of the results, however, are general and should apply to other instruments, such as HIRDLS. To interpret GW patterns in data from such instruments, a detailed knowledge of the sensitivity to different horizontal and vertical wavelengths is essential. In section 2 we derive an analytical approximation for the sensitivity of CRISTA to GWs and compare this to numerical results derived from high spatial resolution radiative transfer calculations. We demonstrate that a two-dimensional consideration of ray paths through the GW structures is imperative. The results prove that CRISTA can detect waves with horizontal wavelength larger than 100–200 km.

[10] In section 3 we describe the CRISTA experiment, data acquisition and analysis. The analysis of GWs in acquired temperatures employs a combination of Maximum Entropy Method (MEM) and Harmonic Analysis (HA), which is well suited for the analysis of monochromatic waves of arbitrary wavelength. The results are compared to those obtained from Fourier transformation and to standard deviations, which highlight the characteristics of the various approaches and the advantages afforded by the MEM/HA analysis.

[11] In section 4, we combine CRISTA data and analysis to isolate enhanced GW temperature amplitudes observed in the stratosphere over southern South America in November 1994. The high spatial resolution in all three dimensions provided by CRISTA [*Offermann et al.*, 1999; *Riese et al.*, 1999; *Grossmann et al.*, 2002] allows us to investigate the three-dimensional structure of the GWs. These investigations are supported by state-of-the-art meteorological nonlinear mesoscale model simulations that act to "hindcast" wave activity here, as well as targeted GW ray-tracing studies. The detailed comparisons underline the necessity to estimate the sensitivity of the limb-sounding technique for understanding the observed GW structures.

## 2. GW Sensitivity Estimation for an Infrared Limb Sounder

[12] For the interpretation of GW data obtained from satellite instruments, detailed knowledge of the instrument's sensitivity to disturbances of different horizontal and vertical wavelengths is essential [*Alexander*, 1998; *Preusse et al.*, 2000]. *Wu and Waters* [1997] and *McLandress et al.* [2000] provided such an analysis for saturated radiances measured by the Microwave Limb Sounder (MLS) on the UARS

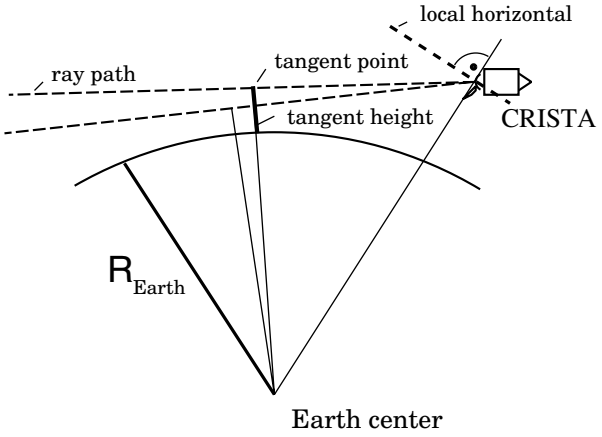


**Figure 1.** Measuring geometry of the limb sounder. Two rays with different tangent heights are shown. These are obtained by tilting the primary mirror of the instrument.

satellite. For optically thin conditions one might estimate an instrument's sensitivity to different vertical scales of GWs based on the vertical weighting function [*Fetzer*, 1990]. Simply speaking, the weighting function defines how much of the observed radiation stems from which part of the atmosphere. One often estimates the visibility of a small-scale disturbance by convolving the disturbance field with the weighting function (this will be discussed later in this section in more detail). To estimate the sensitivity to different horizontal wavelengths $\lambda_x$, one would analogously invoke the horizontal weighting function, which is approximately Gaussian. This gives an amplitude sensitivity

$$S_{A,1D}(\lambda_x) = \frac{A}{A_0} = e^{-2\pi^2\sigma^2/\lambda_x^2} \quad (1)$$

where $A_0$ is the amplitude of the atmospheric wave perturbation, $A$ is the retrieved amplitude, $\lambda_x$ is the horizontal wavelength along the limb direction and $\sigma$ is the width of the horizontal weighting function with typical values of ~200 km. Following (1), a limb sounder has less than 5% sensitivity to a 500 km wavelength GW and shorter waves would vanish completely due to smearing along the ray path. Reasonable sensitivity is found only for horizontal wavelengths longer than ~800 km. This low sensitivity is in obvious contradiction to the mesoscale horizontal structures seen in temperature data from the LIMS and the CRISTA instruments [*Fetzer*, 1990; *Fetzer and Gille*, 1994; *Eckermann and Preusse*, 1999; *Preusse et al.*, 2001b] indicating that (1) does not adequately describe the sensitivity of these instruments to GWs. Thus, here we consider a two-dimensional geometry and generalize the results to three dimensions at the end of the section.

### 2.1. Limb-Sounding Technique

[13] The limb-sounding technique has been described in detail elsewhere [e.g., *Bailey and Gille*, 1986; *Gordley et al.*, 1994; *Marshall et al.*, 1994; *Riese*, 1994; *Riese et al.*, 1999] and is depicted schematically in Figure 1. The satellite views from the orbit position downward through the atmospheric limb. The instrument measures the limb radiance, produced by emission and reabsorption along the ray path. The mathematical description of this radiative transfer is given for example by *Gordley et al.* [1994]. Vertical distributions are obtained by scanning the beam up and down in the atmosphere.

[14] Figure 2 shows the viewing geometry of a limb-sounding instrument projected onto a simulated GW temperature oscillation. Since we use a Cartesian x–z coordinate system, the curvature of the Earth's surface now shows up in form of a curved ray path. If we assume that the atmosphere is optically thin, we can neglect self-absorption in the atmosphere and in this case the intensity measured by the satellite is the sum of all emissions along the ray path. Atmospheric densities increase as we follow the ray path downward. For emitters with constant mixing ratio profiles (e.g., $CO_2$), density increases proportionally as the total air density. Thus, the radiance emitted from a small section along the ray is proportional to the atmospheric density multiplied by the blackbody radiance for the corresponding atmospheric temperature. This emitted radiance is depicted in the upper panel of Figure 2 by the Gaussian curve and shows the weighting that has to be applied to an atmospheric temperature fluctuation in order to obtain the temperature fluctuation detected by the satellite (cf. (1)).

[15] The two ray paths shown in the left panel of Figure 2 reach their lowest altitude at the tangent point at $x = 500$ *km*, where the weighting function peaks. Also given in the upper panel is a horizontal projection of the wave oscillation, showing the horizontal wavelength. As discussed above, a convolution of this wave structure with the weighting function would lead to a nearly complete smearing out of the wave. However, we can observe that the ray path is

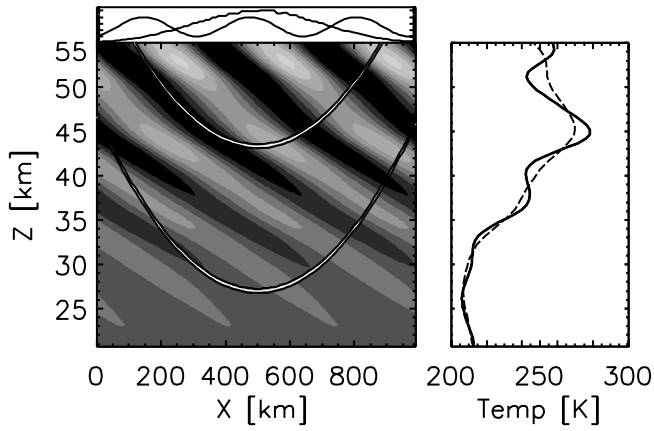


**Figure 2.** Viewing geometry of a limb sounding projected through a simulated GW. Right panel shows the temperature profile used as model input (dashed) and the modeled profile at the tangent point ($x = 500$ km; solid line). The two-dimensional temperature fluctuations and two limb ray paths are shown in the left panel. Top panel gives the weighting function along a ray path and the horizontal waveshape in temperature for the bottom altitude. For details, see text.

partly coaligned along the sloping phase front of the GW at $x$ = 200–400 km. In addition the phase does not change greatly between $x$ = 400 km and the tangent point. Thus, to the left of the tangent point all ray sections with large weight have about the same phase. On the right, phases change rapidly and no net signal can be expected due to averaging along this limb segment. Thus, the phase seen between $x$ = 200 *km* and $x$ = 500 *km* will dominate the radiance attributed to this tangent height. Considering other tangent heights, different phases will be emphasized and a vertical wave oscillation is measured by the satellite instrument.

### 2.2. Analytical Solution of the Radiative Transfer

[16] We can quantify all this by solving the radiative transfer equations analytically given relevant simplifications. The analytical solution not only provides a better understanding of the radiative transfer and the sensitivity to GWs, but also avoids numerical errors due to grid spacing. Thus it can be used for cross checking the results from a full numerical model of the measurement and retrieval as will be done in section 2.3. The analytical solution we will develop uses the following assumptions:

1. The blackbody radiance $B(T)$ can be linearly expanded in the temperature $T$ using a first order Taylor series.
2. The wavelength region considered is optically thin.
3. The background atmosphere is isothermal.
4. The wave amplitude remains constant with altitude.

[17] We first consider the radiance emitted along the ray path. For an optically thin atmosphere we can neglect self-absorption and the limb radiance becomes

$$I = \int_{-\infty}^{\infty} \epsilon(s) B(T(s)) ds, \tag{2}$$

where $s$ is the coordinate along the ray path. The emissivity $\epsilon$ along a small part of the ray is directly proportional to the total atmospheric density $\rho$. Since the density in an isothermal atmosphere is given by $\rho = \rho_0 e^{-z/H}$ we can rewrite this equation as

$$I \sim \int_{-\infty}^{\infty} \rho_0 e^{-z/H} B(T(s)) ds. \tag{3}$$

Thus $W = e^{-z/H}$ is the weight which has to be applied to any atmospheric temperature perturbation to be considered. We now express this weighting function in terms of a horizontal weighting function by replacing $z$ by $s$: Figure 3 shows the geometry of a single tangent ray. In contrast to Figure 2, here the coordinate $s$ is a straight line and the coordinate $x$ follows the Earth's curvature. From Figure 3 we obtain the relations $s = h_l \sin\phi \simeq h_l \phi = x$ and $h_t = h_l \cos\phi \simeq h_l\left(1 - \frac{1}{2}\phi^2\right)$ where $h_l = R_E + z_l$ is the distance from the Earth's center to the considered ray element and $h_t = R_E + z_t$ is the distance to the tangent point. Since $z = z_l - z_t$ we get:

$$z \simeq \frac{s^2}{2h_l} \simeq \frac{s^2}{2R_E}. \tag{4}$$

Our weight takes the shape of a Gaussian

$$W(s) = e^{-s^2/(2HR_E)} \tag{5}$$

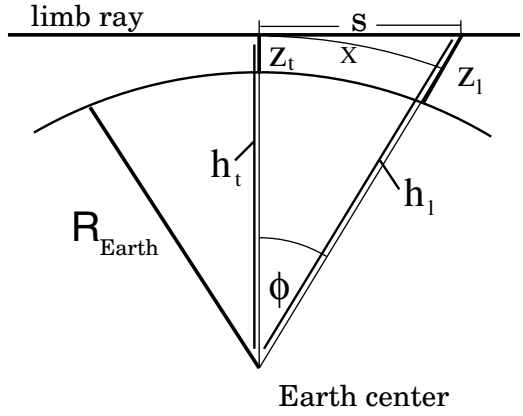


**Figure 3.** Geometry of a single ray path. With varying distance $s$ from the tangent point the altitude $z_l$ of the ray above the Earth's surface and the distance to the Earth's center $h_l = R_{Earth} + z_l$ changes. Tangent height $z_t$, $s$, and $z_l$ can be all connected by trigonometric functions in $\phi$ (see text).

and we obtain $\sigma = \sqrt{HR_E}$. Choosing $H$ = 6.5 *km* and $R_E$ = 6350 *km* we get $\sigma \simeq 200$ *km*, which we have used to evaluate (1).

[18] We now calculate the deviation of the intensity emitted from a sinusoidally perturbed atmosphere from the intensity for the background atmosphere by applying the weighting function. In this step we also linearly expand the blackbody radiation as a function of temperature, which requires small deviations from the mean temperature

$$\Delta I(z_t) \propto \int_{-\infty}^{\infty} W(s)\ A\ \sin(ks + mz + \psi(z_t)) ds, \tag{6}$$

with $A$ being the temperature amplitude and $k = 2\pi/\lambda_x$ and $m = 2\pi/\lambda_z$ being the horizontal and vertical wave numbers, respectively. Thus, after making the approximation $x \simeq s$ the only but important difference between (6) and the assumptions leading to (1) is that (6) contains a height dependence $mz(s)$. This height dependence $z(s)$ is defined by the constraint that the air volumes considered lie along the limb ray. The dependence of the wave phase on tangent height is expressed by the phase $\psi(z_t) = mz_t + \psi_0$. For simplicity we assume here $\psi_0 = 0$ and use (4) to replace $z$ by $s$ and use addition theorems to extract $\psi$ from the integral. In addition, we omit integrals of antisymmetric functions

$$\begin{aligned}\Delta I(z_t) \propto\ & A\cos(mz_t)\int_{-\infty}^{\infty}\cos(ks)\sin\left(m\tfrac{s^2}{2R_E}\right)\exp\left(-\tfrac{s^2}{2HR_E}\right)ds \\ & + A\sin(mz_t)\int_{-\infty}^{\infty}\cos(ks)\cos\left(m\tfrac{s^2}{2R_E}\right)\exp\left(-\tfrac{s^2}{2HR_E}\right)ds\end{aligned} \tag{7}$$

An analytical solution for these integrals exists [*Gradshteyn and Ryzhik*, 1994]. The relative radiance sensitivity is obtained by dividing the intensity variation $\Delta I(z_t)$ by the mean intensity $I(z_t)$ and the atmospheric amplitude $A$. We therefore normalize to the weight

$$\int_{-\infty}^{\infty} \exp\left(-\frac{s^2}{2HR_E}\right) ds = \sqrt{\pi 2HR_E}, \tag{8}$$

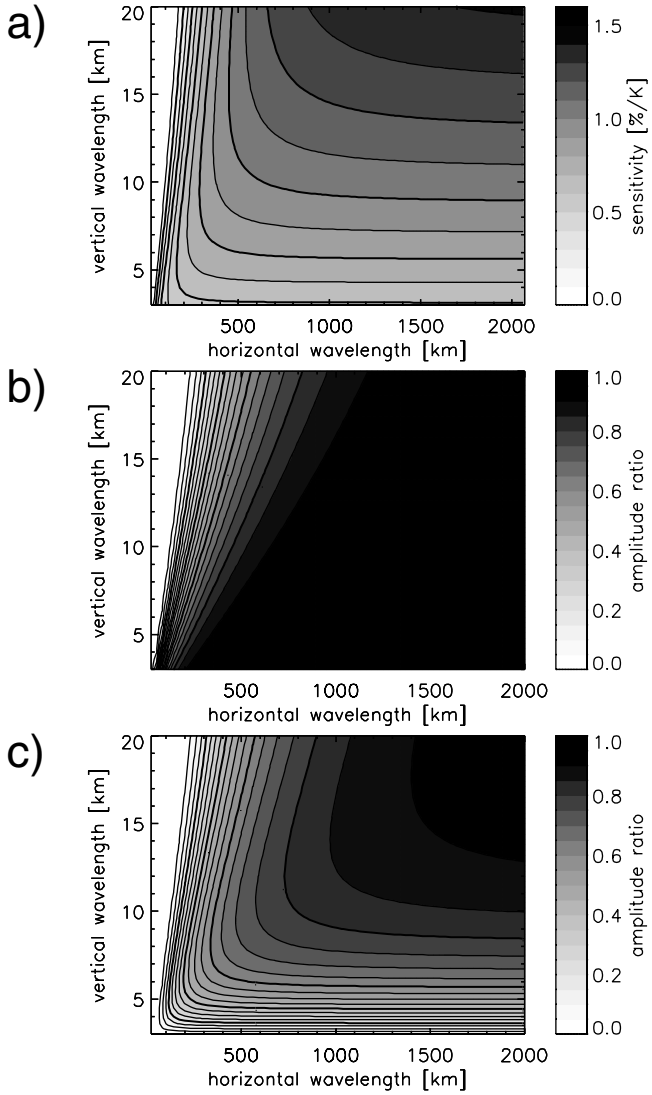


**Figure 4.** Estimated sensitivity of an infrared limb sounder as obtained using an analytical approach. Panel (a) shows the radiance amplitudes as percentage deviations from the total radiance corresponding to an atmospheric oscillation with a 1 K temperature amplitude. Panel (b) gives the ratio of retrieved and atmospheric temperature amplitude for an ''idealized'' retrieval without any restrictions from the instrument. Panel (c) takes sampling effects into account. The same ratio as given in Panel (b) is shown, but as expected for a 3 km step-width onion-peeling retrieval. The plots are based on analytical expressions derived in the text. The contour spacing is 0.1 in Panel (a) and 0.05 in Panels (b) and (c).

and take into account a factor $\frac{1}{B}\frac{\partial B}{\partial T}$ stemming from the linear expansion of the blackbody radiation. We finally obtain the sensitivity of the total ray radiance to a sinusoidal perturbation in the atmosphere:

$$S_{A,2D}(H,k,m) = \frac{1}{B}\frac{\partial B}{\partial T}\sqrt[4]{\frac{c^2}{c^2+a^2}}\ \exp\left(-\frac{cb^2}{4(c^2+a^2)}\right), \quad (9)$$

where $a = m/2R_E = \pi/(\lambda_z R_E)$, $b = k = 2\pi/\lambda_x$ and $c = 1/(2HR_E)$. In order to simulate the CRISTA temperature retrieval we evaluate $\frac{1}{B}\frac{\partial B}{\partial T}$ at 12.6 $\mu m$ wavelength of the IR radiation and at a mean atmospheric temperature of 230 K. The phase shift between the atmospheric wave in temperature and the wave in the limb radiances is

$$\Delta\psi = \frac{1}{2}\arctan\left(\frac{a}{c}\right) - \frac{ab^2}{4(c^2+a^2)}. \quad (10)$$

[19] $S_{A,2D}(H, k, m)$ is plotted in Figure 4a for a constant value of $H = 6.5\ km$. We find that in general short vertical wavelengths are suppressed by the radiative transfer. However, an ''idealized'' retrieval would recover all these degradations in the vertical, given an infinite signal-to-noise ratio of the instrument. We first want to approximate an idealized retrieval, which does not further degrade the measured signals in the vertical, because this allows us to separate the different constraints more clearly. Furthermore, it allows the retrieval step width to be changed easily (see below). Some retrieval algorithms take into account horizontal gradients of the background atmosphere. However, the fine-scale horizontal variations of a mesoscale GW cannot be taken into account in the retrieval process particularly when the viewing direction is not aligned with the flight vector. Thus, the retrieval will recover the wave structure as if it were measured in the absence of any horizontal structure, i.e., for infinite horizontal wavelengths. We can therefore approximate the retrieval by dividing $S_{A,2D}(H, k, m)$ by $S_{A,2D}(H, k = 0, m)$.

[20] Applying this ''idealized'' retrieval we obtain Figure 4b. From this figure we can already see some important features. For vertical wavelengths around 10 km the limb sounder has reasonable sensitivity (0.35), even for wavelengths around 200 km. This is much better than the 1D estimations from (1). We also see that for short horizontal wavelengths (<1000 km) the sensitivity at long vertical wavelengths is diminished. This is an important point for the intercomparison of satellite climatologies [*Preusse et al.*, 2000]. It also explains the low sensitivity predicted by (1). Setting $a = 0$ in (9) we get (1). Thus, the one-dimensional consideration is given by $S_{A,2D}(H, k, m = 0)$ in (9). Figure 2 for this case would show vertically aligned phase fronts and the limb ray can never be oriented parallel to the phase fronts. Thus the one-dimensional estimation (1) is a worst case, which is never found in reality.

[21] From Figure 4b we would expect to see GWs with short vertical wavelengths best. However, this was obtained assuming an ''idealized retrieval'', whereas real retrievals have additional limitations. The smallest resolvable vertical scale visible in the CRISTA data is limited by the vertical sampling and the retrieval process. During the first flight in November 1994, CRISTA sampled with a vertical resolution of 1.5 km [*Riese et al.*, 1999]. However, except for some special observational modes, we have divided the data set into two subsets of 3.0 km vertical step width, which are retrieved separately and reemerged afterward [*Riese et al.*, 1999]. Since a simple onion-peeling scheme is used for the retrieval [*Riese*, 1994; *Riese et al.*, 1999], temperature and trace-gas mixing ratios are interpolated linearly between the altitudes considered. Thus, the retrieval linearly interpolates

throughout any altitude structure which is smaller than the retrieval step width of 3.0 km.

[22] We simulate this in the analytical approach by applying a boxcar filter of the size of the retrieval step width $\Delta z$. The smoothing inherent in the retrieval process is then given by

$$R(\lambda_z) = \frac{\lambda_z\sqrt{2}}{2\pi\Delta z}\sqrt{1-\cos\left(\frac{2\pi\Delta z}{\lambda_z}\right)}. \quad (11)$$

Applying this "cut off" due to the retrieval step to our "idealized retrieved" sensitivity field yields Figure 4c. This results in a realistic decrease in sensitivity at short vertical wavelengths.

### 2.3. High Spatial Resolution Radiative Transfer Calculations

[23] The analytical approach is based on several approximations which may limit the general applicability of the results. A more general approach is provided here by a numerical modeling that is divided into three steps. In the first step a representative background atmosphere is perturbed using a linear two-dimensional (2D) GW oscillation based on WKB theory. Next radiative transfer simulations throughout the model atmosphere are performed leading to vertical radiance profiles such as those measured by CRISTA. (The simulations are idealized in a sense that instrumental error sources such as radiance errors or noise are not taken into account.) The simulated input amplitudes are chosen to be typically a few Kelvin and will be easily identified by the MEM/HA given a reasonable sensitivity value. The third step involves retrieval and data analysis, which are performed following the CRISTA standard data evaluation.

[24] The model used is a two-dimensional, linear WKB model for MWs [*Schoeberl*, 1985]. Horizontal wavelength and altitude profiles of wind speed and potential temperature are input to the model. For our calculations we have chosen a wind profile that is constant with altitude. The value of the horizontal wind speed $U$ sets the vertical wave number $m$

$$|m| = \sqrt{\left(\frac{N}{U}\right)^2 - k^2 - \frac{1}{4H^2}}, \quad (12)$$

where $N$ is the buoyancy frequency, $k$ is the horizontal wave number and $H$ is the scale height. The bottom layer of potential temperature follows the surface topography, which here is sinusoidal. For all other altitudes the displacement of the isentropes is calculated according to linear wave theory. Amplitude growth with altitude follows the WKB relation [e.g., *Lindzen*, 1981]

$$\hat{w}(z) = \hat{w}(0)\sqrt{\frac{m(0)}{m(z)}}\, e^{z/2H} \quad (13)$$

where $\hat{w}$ is the vertical velocity amplitude. In addition, calculations were performed where the density stratification term $e^{z/2H}$ was omitted. The background potential temperature is taken from a zonal mean cross section of CRISTA data extrapolated to the ground and to about 80 km. The extrapolation to 80 km was necessary for the forward radiance calculations.

[25] The primary model output is a perturbed potential temperature field, whereas the radiative transfer calculations are based on temperatures, pressures and trace gases on a geometric altitude grid.

[26] Therefore the atmosphere is rebuilt hydrostatically from the perturbed potential temperature field and temperature and pressure are evaluated. The results are stored on a grid of 10 km in the horizontal and 500 m in the vertical. It should be noted that ozone, which is the most important interfering trace species in the retrieval process, is perturbed by the wave also.

[27] From this model atmosphere we obtain altitude profiles of limb radiances as would be measured by CRISTA with the use of radiative transfer calculations based on the BANDPAK radiance model [*Marshall et al.*, 1994; *Gordley et al.*, 1994]. Every combination of horizontal and vertical wavelength had to be simulated individually. For each profile we define a vertical grid of tangent heights with a spacing of 200 m, oversampling the 1.5 km vertical sampling of the CRISTA instrument. This allows us to convolve the radiances resulting from an infinitesimally thin ray path with the vertical field of view of the CRISTA instrument. For each ray path calculation, the atmosphere is divided into 100 layers. These layers define the spatial resolution of the radiative transfer calculations. The vertical spacing of the layers is dense immediately above the tangent height and increases with altitude. This means highest spatial resolution is obtained where the weighting function peaks. A fine vertical resolution of the layers is especially important for short horizontal wavelengths $\lambda_x$, because in this case the phase of the wave changes rapidly in the x-direction, but close to the tangent point the height of the ray path varies slowly with $x$ (see Figure 2). It turned out that in some cases a vertical resolution of around 30 m is necessary for the layers immediately above the tangent point. At the altitude of each layer the exact position of the ray path is determined and the simulated atmospheric parameters given by the 2D model are interpolated to these ray positions. For these radiative transfer calculations none of the approximations necessary for the analytical approach are made.

[28] The simulated radiance profiles are retrieved using the standard CRISTA retrieval algorithms, including all smoothing procedures [*Riese et al.*, 1999]. Finally the retrieved temperature profiles are analyzed for GWs employing the MEM/HA method described in section 3. The resulting amplitudes and wavelengths can be compared to the input values. To determine the amplitude sensitivity the output of the simulated retrieval is compared to profiles obtained by vertical sections throughout the GW model output at the tangent point.

### 2.4. Results of the Numerical Simulations

[29] Visual inspection of simulated altitude profiles reveals a phase shift between the wave signatures in temperatures extracted directly from the 2D-model solution and those obtained by simulated radiative transfer and retrieval. These phase shifts $\delta\phi(z)$ depend on the background atmosphere and hence on the altitude. This can be noted from (10), where $\Delta\psi$ depends on the scale height $H$ via $c$.

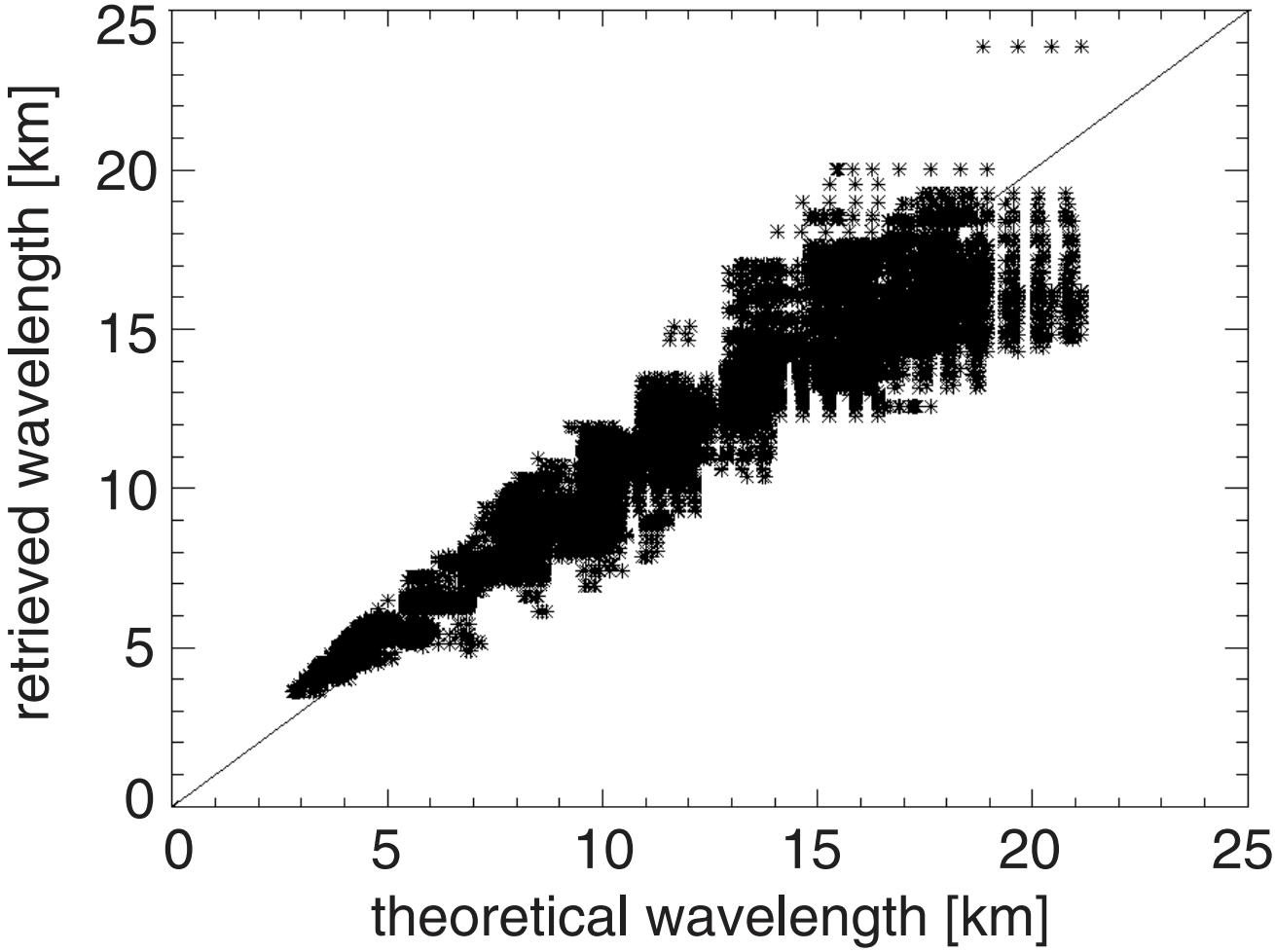


**Figure 5.** Scatterplot of retrieved versus theoretical vertical wavelength. The solid line indicates a perfect retrieval of the vertical wavelength. The observed scatter of the singular points as retrieved from simulated CRISTA profiles is due to radiative transfer effects and the analysis method. The scatter gives a good indication of the precision of the vertical wavelength retrieved from real CRISTA measurements.

To demonstrate the way in which height dependent phase shifts can alter the vertical wavelength, we consider a sinusoidal wave in a single retrieved profile $T' = \hat{T} \sin(mz + \phi + \delta\phi(z)) = \hat{T} \sin \psi$, with $\phi$ being the phase at $z = 0$. For example, if the phase shift $\delta\phi(z)$ in a certain altitude range decreases, the total phase $\psi$ of the wave changes more slowly than we would expect from the vertical wave number $m$. This results in an apparently longer vertical wavelength in the retrieved temperatures and by the same token an increasing phase shift results in a shorter wavelength. This variation of the vertical wavelength is shown in Figure 5. The vertical wavelength deduced from the retrieved temperatures is compared to the input wavelength from (12). We find a scatter of $\sim$20% in retrieved wavelengths.

[30] The simulations employed to produce Figure 5 are based on a zonal mean background atmosphere and therefore embody realistic geographical variations. In addition, the same method as used here is also used to determine the vertical wavelength of GWs observed in real flight profiles (see section 3). Thus, the scatter observed in Figure 5 represents physical effects from the radiative transfer as well as influences of the analysis method and is a good estimate of the precision of the vertical wavelength retrieved from CRISTA temperatures.

[31] GW simulations were performed for constant amplitudes and amplitudes growing exponentially with height. In the real atmosphere both cases are likely to be observed. Exponential growth is expected where GWs propagate conservatively without interaction with the background flow. A constant amplitude reflects the classical case described by *Lindzen* [1981], where GWs are breaking and retain their saturation amplitude. It should further be noted that even in the case of exponential growth the amplitude increases with twice the scale height of the density decrease. Thus, the weight along the ray path decreases faster than the wave amplitude increases and the total contribution to the measured radiance decreases exponentially with altitude. Results from growing amplitude as well as constant amplitude simulations are shown in Figure 6. Panel (a) reproduces Figure 4c. Panels (b) and (c) show results for constant amplitude and exponentially increasing amplitude waves, respectively. The values of the numerical simulations are an average over altitudes of 25–60 km and 13 latitude bins. This average increases the statistical significance of the

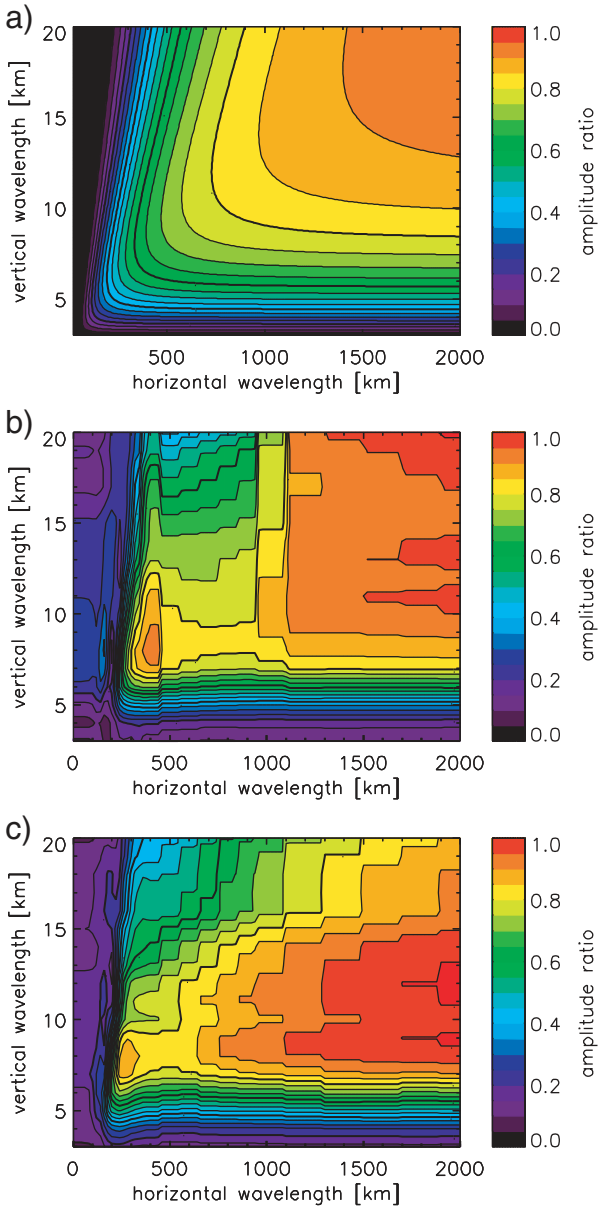


**Figure 6.** Estimated sensitivity of retrieved CRISTA temperatures to GW oscillations. Radiative transfer as well as retrieval effects are included. Panel (a) reproduces Figure 4c. Panels (b) and (c) show the results of the numerical simulations with constant GW amplitudes and amplitudes growing exponentially with altitude, respectively. All three figures exhibit the same salient features, particularly the strong decrease of sensitivity at around 200 km horizontal wavelength and the decreased sensitivity to long vertical wavelength for a given horizontal wavelength. Panels (b) and (c) are very similar in the horizontal wavelength range from 300 to 800 km, allowing us to deduce a one-dimensional correction factor, which can be applied to measured CRISTA data.

given values. The three panels have the same salient features, specifically a strong decrease of sensitivity at $\lambda_x \approx 200$ km and a decrease of sensitivity at long vertical wavelengths for a given horizontal wavelength. The results of the full numerical modeling (Panels (b) and (c)) reveal an "island" of high sensitivity at $\lambda_x \approx 350$ km and $\lambda_z \approx 6-8$ km vertical wavelength, which is not found in the analytical solution. For horizontal wavelengths between 300 and 800 km, Panels (b) and (c) agree reasonably and exhibit only weak dependence on the horizontal wavelength. Thus, a one-dimensional sensitivity function averaged over the 300–800 km horizontal wavelength range and depending solely on the vertical wavelength is representative of the waves contained in the residual temperatures. This is an important point, because it allows us to correct amplitudes retrieved from CRISTA measurements for visibility effects noted in Figures 4 and 6 [see also *Preusse et al.*, 2000]. This would not be possible if a strong dependence on horizontal wavelength was present, since it is often difficult to deduce the horizontal wavelengths as will be seen in section 4. We will discuss in section 3.3 to what extent the assumption is valid that horizontal wavelengths are shorter than 1000 km.

[32] It should be noted that there is an artificial background of relatively high sensitivity (0.2) at very short horizontal wavelengths. This is spurious and due to a vertical spacing of the forward calculations that is still too coarse. Inspection of single profiles indicated that the altitude layering has to be even finer than the 30 m spacing we have used for these simulations. Here the analytical approach, which is not restricted by numerical errors and grid spacing, supports the finding of vanishing sensitivity to the very short horizontal scales less than about 200 km. For longer horizontal wavelengths the numerical modeling can be expected to yield reliable results.

[33] So far we have discussed sensitivity variations versus wavelength. However, an important question is whether the observational technique itself can cause artificial geographical structures in the observed GW variances. Thus, we now keep the horizontal and vertical wavelength fixed by averaging all values in a box of $\lambda_x = 300-800$ km and $\lambda_z = 8-12$ km. Figure 7a plots these values versus latitude and altitude. A second wavelength box of $\lambda_x = 300-800$ km and $\lambda_z = 15-20$ km results in the distribution shown in Figure 7b. It should be noted that the MEM/HA method results in wave amplitudes which are independent of the phase of the wave relative to the analysis interval. In addition, the average of $\lambda_x = 300-800$ km and different vertical wavelengths is also an average over different phases of the waves. The observed structures are therefore reliable and not due to a specific phase choice made when initializing the simulations. The observed geographical dependence is small for the short vertical wavelengths (Panel a) and varies by up to ±30% for the longer vertical wavelengths shown in Panel (b). However, this higher value corresponds to about 2 dB for squared amplitudes and we will show in section 3 and the companion paper (Preusse et al., in preparation, 2002) that these variations are small compared to the observed geophysical variations of GW variances.

[34] One last point is whether there are changes in the phase of the observed waves. The analytical approach indicates that the radiative transfer (10) as well as the retrieval induce phase shifts. These are expected mostly where the radiance sensitivity is small, namely for

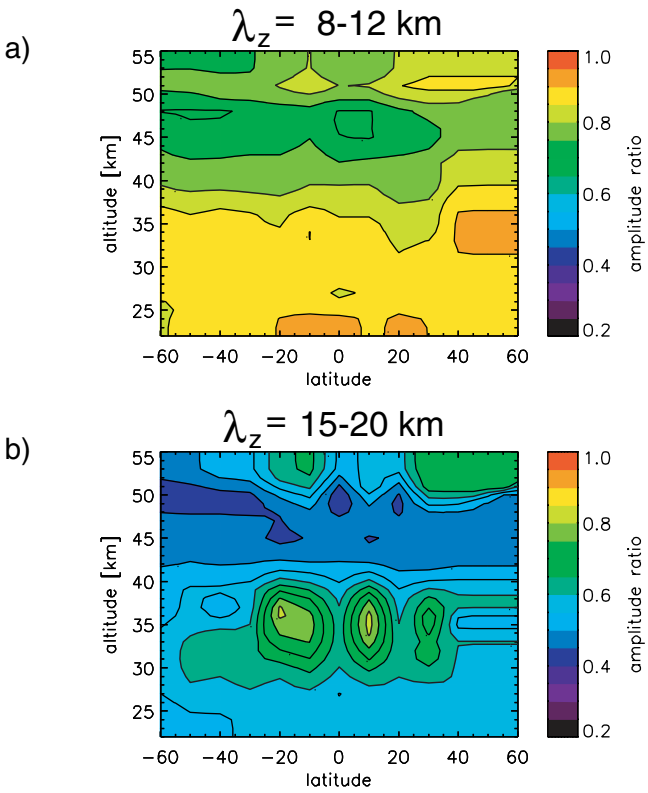


**Figure 7.** Dependence of the sensitivity on the location of the measurement. Short vertical wavelengths ($\lambda_z$ = 8–12 km) given in Panel (a) depend only weakly on altitude and are nearly independent of latitude. The geographical dependence of the longer vertical wavelengths ($\lambda_z$ = 15–20 km) is stronger. However, as shown in sections 3 and 5, the observed variations in GW activity are much stronger.

short vertical and short horizontal wavelengths (compare Figures 4 and 6). Results from numerical simulations are shown in Figure 8, which plots the absolute values of the phase differences between 2D-model wave input and retrieved temperature profiles. These phase shifts are small for most combinations of horizontal and vertical wavelength. The phase shifts therefore do not prevent us from deriving horizontal wave structures from the CRISTA temperature data.

### 2.5. Generalization to Three Dimensions

[35] The sensitivity estimates shown in Figures 4 and 6 are based on two-dimensional radiative transfer calculations. However, the real atmosphere is three dimensional and it is likely that the instrument views waves at various angles. This is illustrated in Figure 9, which shows the horizontal projection of a limb ray and the horizontal phase fronts of a GW. The horizontal wavelength along the line of sight (LOS) is a factor 1/(cos $\alpha$) larger than the real horizontal wavelength $\lambda_x$. Thus, for waves viewed at an angle $\alpha$ to the phase fronts we have to scale the x-axes of Figures 4 and 6 by cos($\alpha$). Taking $\alpha = 60°$ as an example, the shortest horizontal wavelength $\lambda_x$ for which the sensitivity is larger than 0.5 is now 100–120 km instead of 200–240 km in the two-dimensional calculations (Figures 6b and 6c), which tacitly assume $\alpha = 0$.

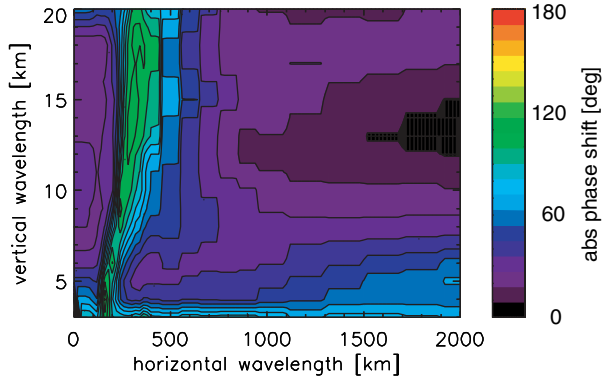


**Figure 8.** Phase shift due to the radiative transfer. The values are mostly small except for wavelengths, for which the small sensitivities have been found in Figure 6.

[36] We can assume that the case where the LOS is coaligned with the horizontal wave vector is the exception and that nonzero view angles $\alpha$ frequently occur. Thus, a fraction of the atmospheric waves with horizontal wavelengths between 100 km and 200 km is observed by the limb viewer. How large this fraction is may depend on a possible general preference of the wave propagation direction and the actual view direction of the instrument. This is discussed in some detail in section 4. However, for very large view angles $\alpha$ this relation may not hold any longer because this would assume infinite plane horizontal wave fronts.

[37] Employing the one-dimensional correction function [*Preusse et al.*, 2000] one can rescale the measured GW amplitudes to estimate the "true" atmospheric amplitudes of mesoscale GWs with vertical wavelengths $\lambda_z \gtrsim 5$ km. The decrease of sensitivity at the short horizontal wave-

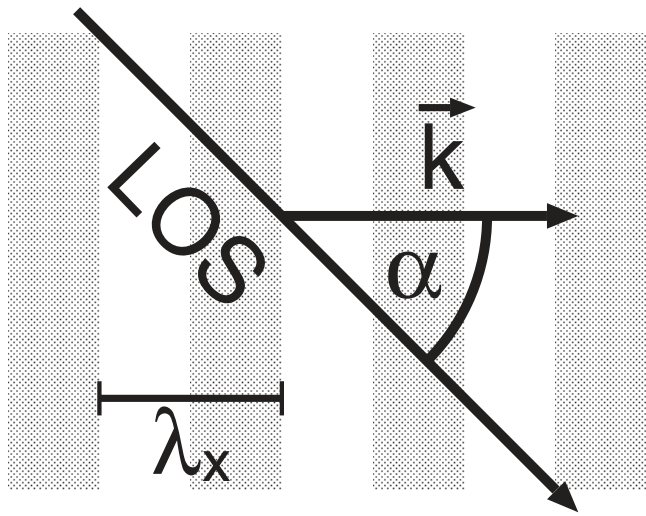


**Figure 9.** Horizontal projection of an arbitrarily oriented GW and the line of sight (LOS). Instead of viewing perpendicular to the wave fronts (gray shading), there is an angle $\alpha$ between the line of sight and the horizontal wave vector $\vec{k}$.

length edge is very steep and we therefore can assume that a wave is either scaled correctly or not measured at all. The importance of rescaling the measured amplitudes is pointed out by *Preusse et al.* [2000].

## 3. Data Acquisition and Analysis

[38] We have shown in the previous section that mesoscale GWs cause detectable signatures in temperature altitude profiles acquired by an infrared emission limb sounder. Such vertical temperature profiles were sampled by the CRISTA instrument with high spatial resolution and nearly global coverage. In this section we briefly introduce the instrument and discuss the mathematical tools used to analyze the data to extract the vertical wavelength, amplitude and phase of GW oscillations in acquired temperature profiles.

### 3.1. Measurement Technique and Detrending

[39] The CRISTA instrument was designed to acquire very high spatial resolution data. For this purpose CRISTA uses three telescopes viewing 18° apart to measure height profiles of thermal emission limb spectra in the middle and far infrared at a spectral resolution of about 500 [*Offermann et al.*, 1999]. The instrument was successfully flown during two space shuttle missions, STS 66 (November 1994) and STS 85 (August 1997), here referred to as CRISTA-1 and CRISTA-2, respectively. Detailed information on the first mission can be found in the works of *Offermann et al.* [1999] and *Riese et al.* [1999]. The second mission is described by *Grossmann et al.* [2002]. On both flights the spacecraft orbited at 300 km altitude with a 57° inclination. This results in ~16 orbits a day. Observations range from ~57°S to ~65°N and from ~72°S to ~72°N during CRISTA-1 and CRISTA-2, respectively.

[40] The retrievals of stratospheric temperatures from $CO_2$ band emissions around 12.6 μm and mesospheric temperatures from the 15 μm $CO_2$ band are described by *Riese et al.* [1999]. The vertical sampling steps are 1.5 km and 2.0 km for CRISTA-1 and CRISTA-2, respectively. Given a sampling time of ~1 s per spectrum, a complete altitude profile consisting of 20 to 43 altitude steps is obtained in 25 to 50 s depending on the measuring mode. The lower boundary of the stratospheric measurements was 15 km for CRISTA-1. The upper boundary depends on measuring mode. For an overview of the different measuring modes, see the works of *Riese et al.* [1999] and *Grossmann et al.* [2002] for CRISTA-1 and CRISTA-2 observing modes, respectively. In the stratosphere and lower mesosphere the precision of the retrieved temperature data was estimated to be better than 0.4 K for both missions.

[41] To obtain residual temperature fluctuations, retrieved temperature data were detrended by subtracting a background atmosphere estimated by a Kalman filter. Common modes of planetary waves in the stratosphere are expected to have zonal wave numbers up to 4 and inspection of CRISTA data shows no significant contributions from higher wave numbers (Oberheide, personal communication, 2001). Thus a 0–6 wave number Kalman filter [*Rodgers*, 1977; *Ern*, 1993] should account for all planetary wave structures in the background [*Fetzer and Gille*, 1994; *Preusse et al.*, 2001a]. In addition, ascending and descending orbit nodes are treated separately to take into account tidal structures, which become important in the mesosphere [*Ward et al.*, 1999; *Oberheide et al.*, 2000].

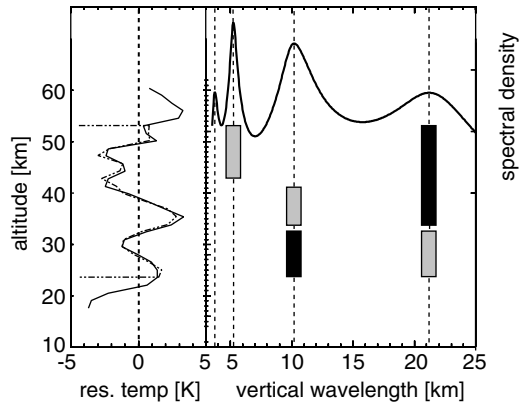


**Figure 10.** Example of the combined MEM and HA. The left panel shows an altitude profile of measured CRISTA temperature residuals (solid) and the reconstruction from the fit (dashed). The profile was acquired on 9 November, eastward of Chile at 24°S and 82°W. The right panel plots its detrended MEM spectrum, the spectral peaks (bottom to top vertical lines), and the two leading amplitudes (solid and hatched bars). Spectral density scale is logarithmic.

[42] The Kalman filter is estimated on a regular altitude grid of 1.5 km spacing. The coefficients are estimated for latitude bands of 0.5° and smoothed afterward with a 7-point running mean in latitude. The application of the Kalman filter to the CRISTA data is described in detail by *Ern* [1993]. A comparison of nonfiltered and Kalman-filtered CRISTA data was presented by *Offermann et al.* [1999].

[43] The background temperature estimated by the Kalman filter is interpolated in altitude and latitude to the precise measurement locations of the individual height profiles. It should be noted that the estimation of the Kalman filter coefficients is performed on each altitude layer separately. Therefore no degradation of the vertical resolution of local fluctuations should result from this detrending.

### 3.2. Analysis Method

[44] Height profiles of Kalman detrended residual temperature fluctuations are analyzed by a combination of MEM [*Press et al.*, 1992] and HA as illustrated in Figure 10. The left panel shows the Kalman detrended vertical temperature profile as the solid curve. This profile is spectrally analyzed using MEM. The MEM is performed on the complete height profile, but can also identify wave contributions visible only at subintervals of the profile. A spectrum obtained by MEM generally has a red noise contribution which particularly interferes with the spectral components of interest, if the number of data points in a given analyzed data set is low. Thus, weak or broad peaks may be difficult to detect in the presence of the red noise background. Therefore we here detrend the MEM spectrum by a quadratic fit through the minima of the spectrum. This detrended MEM spectrum

is given in the right panel of Figure 10. Thin dashed vertical lines indicate the maxima in the spectrum as identified by a peak finding algorithm. These wavelength peaks are the basis of the HA performed on a sliding interval shifted in steps of one sampling point through the profile. In an iterative process the points in the sliding interval are fitted by sinusoids and the wave with the largest amplitude is removed from the data. The two largest amplitudes so obtained and their corresponding wavelengths and phases are attributed to the central altitude of the sliding interval. It should be noted that in the case of double peaks, which can occur if an MEM is applied to a small data set [*Press et al.*, 1992], all the wave amplitude is attributed to one of the two peaks. This is due to the subtraction of the fitted wave from the data before applying the next fit. Hence the second largest amplitude stored for further investigations will contain an independent wave contribution.

[45] The solid dark and hatched bars in the right panel of Figure 10 indicate the wavelength belonging to the strongest and second strongest amplitude in the profile on the left, respectively. For example, the two temperature maxima at around 25 km and 35 km altitude correspond to a dominating wavelength of about 10 km in the lower altitudes. The major contribution at higher altitudes has a very long wavelength (≈21 km) visible as a very wide trough at around 45 km. Above 43 km the second wave component captures a short wavelength contribution of around 5 km vertical wavelength. The dashed curve in the left panel shows the profile reconstructed from the two wave components with the strongest amplitudes, evaluated at each altitude step from the MEM/HA values. It can be seen that the profile is locally well described by two wave components which may vary with altitude.

[46] The example given in Figure 10 is, however, not really typical. Normally the altitude profiles look less rich and only two wavelengths are identified by the MEM. These profiles can be even more accurately described by the MEM/HA decomposition.

[47] Since for each amplitude value the corresponding vertical wavelength is known, the results can be corrected for degradation due to retrieval and radiative transport following the method described in section 2.4.

### 3.3. Method Intercomparison

[48] The MEM/HA analysis method assumes that two monochromatic waves specify almost completely the spectral distribution of wave energy in the vertical direction in every profile. For two-dimensional MWs this is often a reasonable assumption, because the vertical wavelength is governed by the buoyancy frequency and the wind speed only [*Queney*, 1948; *Eckermann and Preusse*, 1999]. In addition, there are indications from lidar measurements, rocket soundings, radiosondes and radar measurements that a few monochromatic wave components are sufficient to describe the observed temperature fluctuations [e.g., *Cot and Barat*, 1986; *Riggin et al.*, 1995; *Sica and Russell*, 1999; *Bittner et al.*, 1997]. However, we also investigated the general applicability of the method for satellite GW analysis on a statistical basis. Here we compare the results of the MEM/HA to those obtained by a Fourier Transform (FT) on a sliding window and to conventional standard deviations, the latter as used by *Fetzer and Gille* [1994].

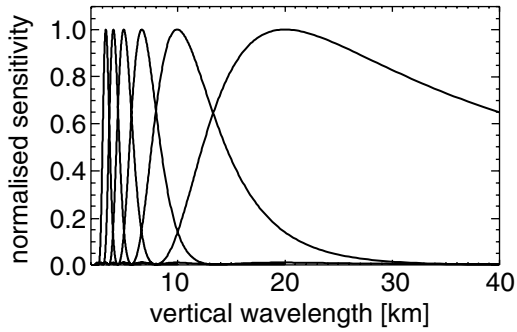


**Figure 11.** Leakage functions for a 13-point Fourier transform at 1.5 km vertical sampling. The longest vertical wavelength is about 20 km and the shortest wavelength is $20/6 \approx 3.3$ km.

[49] While the length of the sliding window of the MEM/HA can be chosen almost arbitrarily, the length of the sliding window used for the FT is directly coupled to the wavelengths resolved by the FT. For this comparison we use a 13-point window which is equivalent to an interval length of ~20 km, given a 1.5 km sampling in altitude. To suppress leakage, a Welch window is applied to the data before the FT. The spectral power is normalized utilizing Parseval's theorem [*Press et al.*, 1992]. Figure 11 shows the leakage functions of the different Fourier components dependent on the vertical wavelength calculated according to *Press et al.* [1992]. These functions quantify the leakage between the several wavelength bins, i.e., they show the magnitude of the contribution from other wavelengths to the considered wavelength bin. The wavelengths of maximum sensitivity (centers of the wavelength bins) are given by integer fractions of the length of the analysis interval.

[50] We first compare the results of the Fourier transform to the zonal mean standard deviations calculated from Kalman-detrended temperature fluctuations. Since Parseval's theorem has been used to normalize the results of the FT for a stationary process we would expect the standard deviations to agree with the sum of the spectral energy of all frequency bins. In Figure 12 we compare the standard deviations (Panel a) with the sum of spectral energy obtained from the FT method (Panel b). Both are given in dB over 1 $K^2$ ranging from 0 to 15 dB. Panel (c) gives the ratio between the standard deviation and the FT variances. At altitudes higher than about 30 km the patterns in Panels (a) and (b) are very similar. Thus, on average the ratio is close to 1 and small-scale patterns range from 0.7 to 1.2. Around 25 km we observe that the FT values are much higher. This is due to the vertical width of the sliding analysis window. A value obtained by the FT method that is attributed to 25 km contains contributions from a band of altitudes between 15 km and 35 km. In particular the lower boundary here is problematic because of the very enhanced tropical maximum in the standard deviations observed between 15 km and 20 km altitude (Figure 12a). The FT projects this maximum to higher altitudes. In addition, the subtropical minima are shifted in altitude and smeared out.

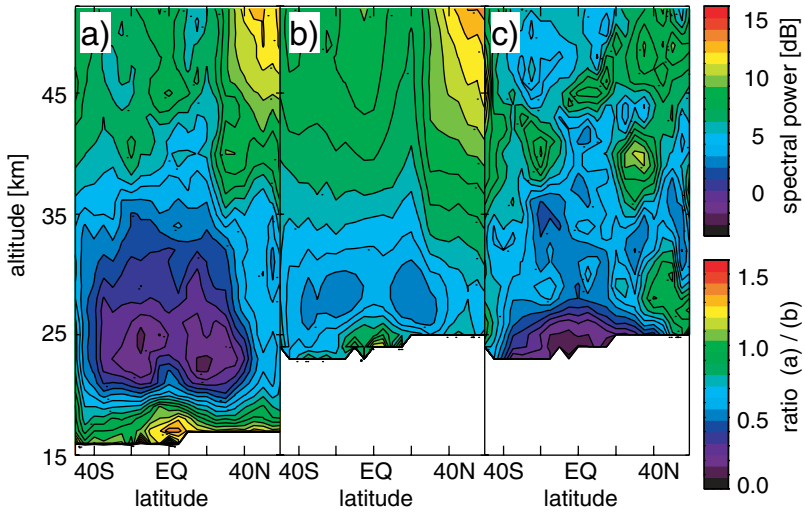


**Figure 12.** Comparison of standard deviations (a) with the sum of the square of the amplitudes of all spectral bins calculated by the Fourier transformation (b). Panel (c) gives the ratio of Panel (a) divided by Panel (b). For details, see text.

Thus, at the lowermost heights of ~25 km the ratio shown in Figure 12b approaches zero. One should keep this weakness of the FT in mind when comparing these results with those of the MEM/HA.

[51] To give a realistic impression of the relation of GW variance contained in the several wavelength ranges, visibility corrections as deduced in section 2.4 are applied. The FT wavelength bins are corrected with scaling factors according to their center wavelengths, the amplitudes obtained from MEM/HA are scaled individually as described in section 3.2. In contrast to the FT the wavelength ranges of zonal means calculated from MEM/HA results can be chosen arbitrarily. In Figure 13 we compare the results of the FT (uppermost row) to those obtained by a MEM/HA with interval lengths of 9 points (13 km; middle row) and 5 points (7.5 km; lowermost row). The left column compares the FT wavelength bin centered at 20 km (Panel (a)) with MEM/HA results in the range from 15 km to 30 km vertical wavelength (Panels (d) and (g)). The middle and right columns compare the sum of all FT bins with center wavelengths shorter than 10 km (b) and 6.7 km (c), respectively, to MEM/HA results in the wavelength ranges of 3.0–15.0 km (e, h) and of 3.0–10.0 km (f, i). Good agreement between FT and MEM/HA variances is found for altitudes above 30 km. However, the deviations below 30 km are as expected because the analysis interval of the MEM/HA is much smaller than the sliding window of the FT and the vertical smearing effects are much less of a problem using MEM/HA. Particularly low smearing effects are found (cf. standard deviations in Figure 12) when we reduce the window length of the HA from 9 points (13 km; middle row) to 5 points (7.5 km; lowermost row). The comparison shows that a 7.5 km interval length results in reliable zonal mean values even in the 15–30 km vertical wavelength range.

[52] It should be noted that both methods exhibit a pronounced tropical maximum and subtropical minima in the lower stratosphere only for short vertical wavelengths. This is an important issue when comparing GW climatologies based on different satellite instruments [*Preusse et al.*, 2000]. The fact that we observe the tropical maximum only at short vertical wavelengths may be related to the higher occurrence of low frequency and long horizontal wavelength waves in the equatorial region [*Alexander et al.*, 2002]. These long horizontal wavelengths in the tropics induce errors when the scaling function is applied. The deduction of the scaling function is based on the assumption that the horizontal wavelength of the waves is of the order of 1000 km or shorter. This is not generally true in the tropics. At low vertical wavelengths the reduced sensitivity is mainly due to the retrieval process. Thus, it does not depend on the horizontal wavelength, as can be seen from Figures 4 and 6. At long vertical wavelength the radiative transfer causes reduced sensitivity values and a strong dependence on the horizontal wavelength is observed. This leads to an overcorrection of the waves with both long horizontal and long vertical wavelengths, and hence to an overestimation of the tropical wave activity shown in the left column of Figure 13.

[53] From the results presented in Figures 12 and 13 we conclude that the MEM/HA provides reliable information on GW temperature variance for variable choices of wavelength intervals. It is superior to the FT method in dealing with nonstationary wavelengths and amplitudes in profiles. We also find that a 9-point sliding window is sufficient for analyzing waves with wavelengths longer than 20 km. The reliability of the results is further supported by the excellent agreement between results from GPS/MET [*Tsuda et al.*, 2000] and MEM/HA amplitudes inferred from CRISTA data [*Preusse et al.*, 2000].

## 4. Case Study: Stratospheric GWs Measured Above South America

[54] Previous investigations of CRISTA-1 temperature data by *Preusse et al.* [1999] and *Eckermann and Preusse* [1999] have shown that on day 310 (6 November 1994) very large amplitude GWs were observed over the southern

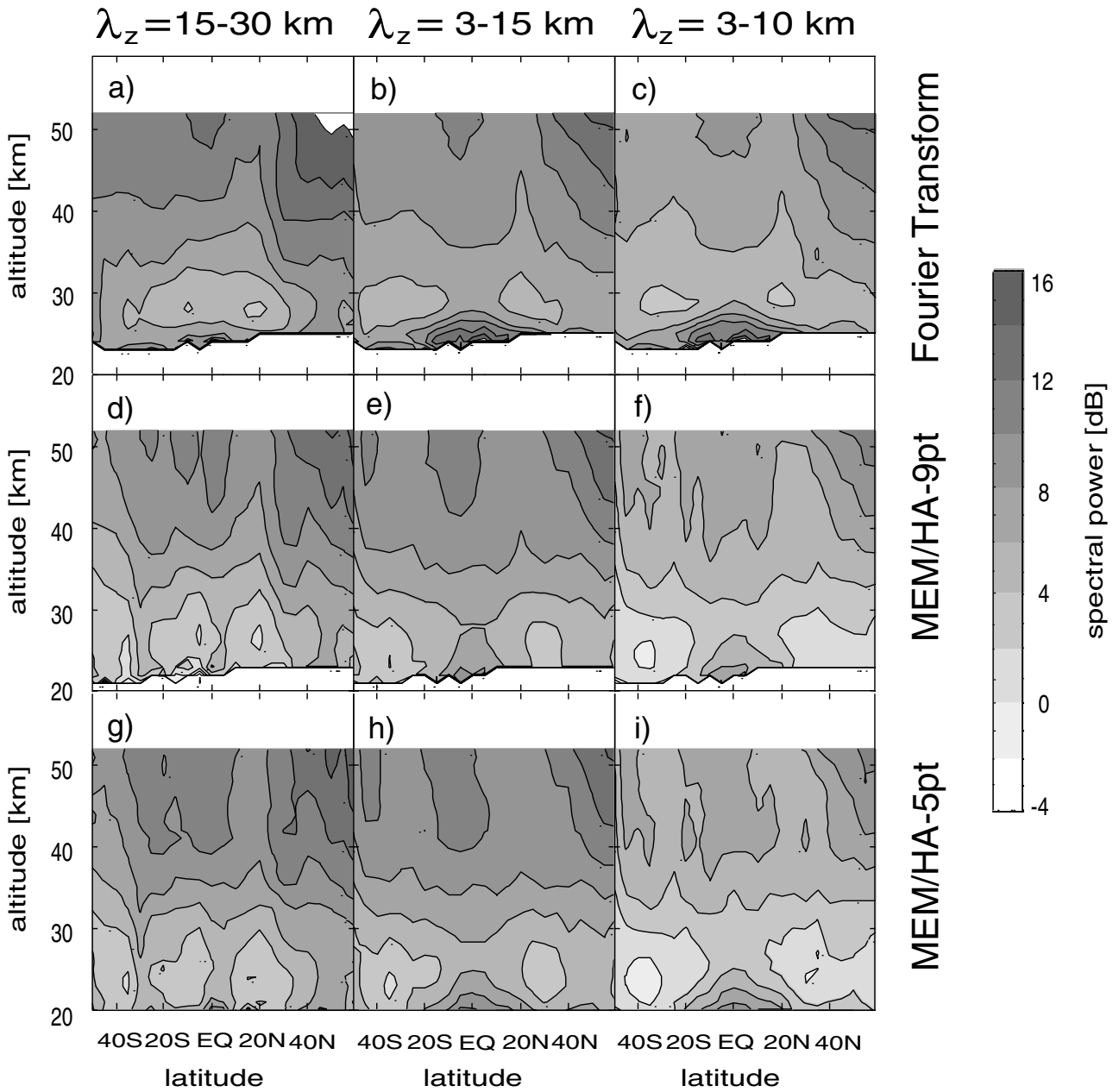


**Figure 13.** Comparison of zonal mean spectral power in CRISTA residual temperatures using FT (upper row) and MEM/HA on a 9 point (middle row) and 5 point (lowermost row) sliding window for different wavelength ranges (different columns). In general, the agreement is good, but the MEM/HA provides better altitude resolution and thus reproduces the tropical maximum at more realistical altitudes (compare also Figure 12; for details, see text).

tip of South America. *Eckermann and Preusse* [1999] attributed the enhanced perturbations to MWs forced by flow over the Andes. They compared a time series of four consecutive days of CRISTA-1 data from this region to hindcasts of the Naval Research Laboratory Mountain Wave Forecast Model (NRL-MWFM). It has been shown that the model was able to reproduce the day-to-day variations in GW activity. However, the NRL-MWFM results were concentrated over the mountain ridge, while enhanced fluctuations in the CRISTA data extend further to the lee side and beyond the very southern tip of South America toward the ocean. In addition there was a study by *Tan and Eckermann* [2000] based on a two-dimensional nonlinear high resolution model. However, to address the full horizontal structure of the GW field in this region a different kind of simulation has to be used. We therefore simulate waves above South America on this day by employing a three-dimensional mesoscale model.

### 4.1. Comparison With the MM5 Mesoscale Model

[55] The model we use is the fifth generation Pennsylvania State University (PSU)/National Center for Atmospheric

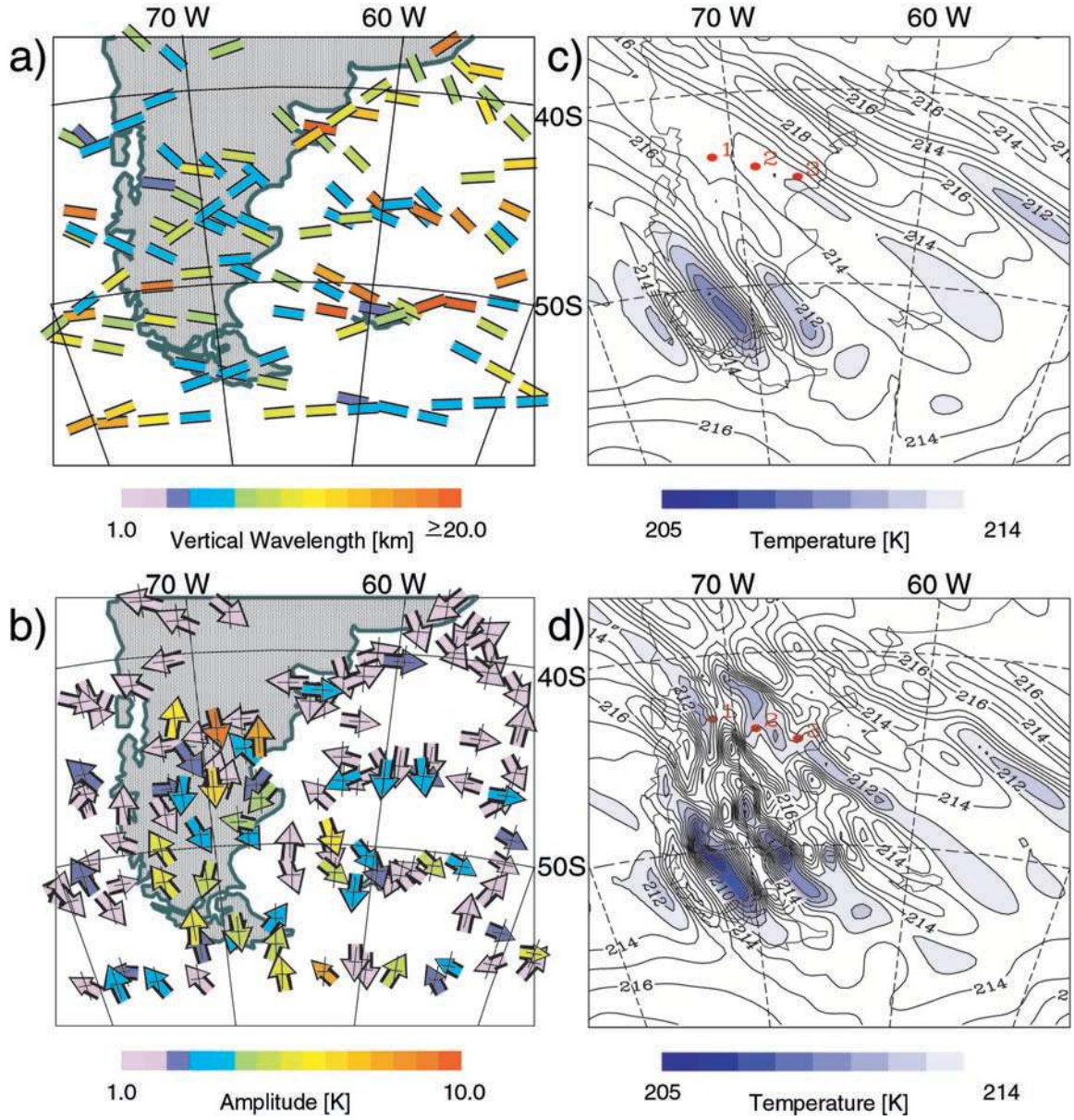


**Figure 14.** GW activity over South America on 6 November 1994 at a pressure surface of 30 hPa. The vertical wavelength measured by CRISTA and the viewing direction of the instrument are shown in Panel (a). The wavelength information is significant only for waves with amplitudes $\gtrsim 1.5$ K. The wave amplitudes are shown in Panel (b) together with the phase of the waves, which is indicated by the direction of the arrows. An upward-pointing arrow indicates 0° and increasing phase is indicated by counterclockwise rotation. Panel (c) shows the temperature field at 30 hPa as simulated by MM5 and Panel (d) shows MM5 results using a nested grid to increase the horizontal resolution. Only the run with enhanced resolution exhibits pronounced wave structures at the red dots, which give the location of the three strong amplitude profiles visible in Panel (b). For details, see text.

Research (NCAR) mesoscale model MM5 [*Dudhia*, 1993; *Grell et al.*, 1994]. The model integrates the fully compressible set of fluid equations in a rotating frame of reference. In the nonhydrostatic version used here velocity, pressure perturbation and temperature are the prognostic variables. The model domain is centered around 65°W and 45°S with a horizontal domain size of 3000 km × 3000 km. A local grid refinement (nested domain of 1210 km × 1210 km) covers the mountain ridge on the west side of South America. The horizontal mesh size of the outer domain is $\Delta x = 30$ km, the grid length of the nested domain is 10 km.

[56] The vertical resolution $\Delta z$ is ∼260 m. In total, 99 levels are used up to the model top at 10 hPa (∼28 km), where a radiative boundary condition avoids spurious downward reflection of vertically propagating GWs. Radiative and moist processes are switched off as the prime concern is the dynamics of MWs at upper levels. The initial conditions and boundary values of the model integration

were prescribed by 6-hourly analyses of the European Center for Medium-Range Weather Forecasts (ECMWF) with a horizontal resolution of 1.125° in latitude and longitude and 15 levels between the surface and 10 hPa. This model setup has been successfully used for simulating stratospheric waves above Scandinavia and southern Greenland [*Dörnbrack et al.*, 1998, 1999; *Leutbecher*, 1998; *Dörnbrack and Leutbecher*, 2001]. The model simulation starts on 5 November at 0000 GMT. Data shown here are simulated for 6 November 0600 GMT, which is closest to the CRISTA-observations. Thus, the model had already run for 30 h, when the data shown here were extracted.

[57] Figure 14 compares the CRISTA data with the results from the MM5 model results at a pressure level of 30 hPa (∼24 km altitude). Figure 14a shows a map of MEM/HA temperature perturbations from CRISTA. The color code gives the vertical wavelength, and the alignment of the lines indicates the viewing direction of the telescope. Figure 14b shows the corresponding amplitudes of the waves and the arrow directions indicate their phases. The phases are determined by the MEM/HA from the vertical wave structure with an upward-pointing coordinate and $z$ = 0 at the plotting altitude. A northward-pointing arrow indicates 0° and increasing phase is indicated by counterclockwise rotation of the arrow. (This means: 90° = westward-pointing, 180° = southward-pointing, 270° = eastward-pointing).

[58] If the CRISTA sampling is sufficiently dense in the horizontal to resolve the direction of the phase turn, we can infer the tilt of the wave fronts in the vertical, because these phase estimates contain vertical information. For example, a phase increasing from west to east (counterclockwise rotation) indicates a westward tilt of the phase fronts. The underlying black crosses indicate the locations of the tangent points. Panels (c) and (d) give results from hindcast simulations using the MM5 model which will be discussed below.

[59] On the upwind (westward) side of the Andes negligible amplitudes are observed in Figure 14b. The corresponding wavelength information in Figure 14a is insignificant for profiles with amplitude $\hat{T} < 1$ K. Enhanced GW amplitudes are observed above and downwind (eastward) of the landmass, but not further northward than ∼40°S. This can be explained by considering the dispersion relation. For a two-dimensional hydrostatic MW in a constant background atmosphere and neglecting the Coriolis force the theoretical vertical wavelength is given from (12) by

$$\lambda_{z,2D}^2 = \frac{(2\pi)^2}{N^2/U^2 - 1/(4H^2)} \approx \frac{4\pi^2 U^2}{N^2} \qquad (14)$$

with $N$ the buoyancy frequency and $H$ the scale height. If the angle $\Phi$ between the wind direction and the horizontal wave vector differs from 180°, i.e., if the wind direction is not perpendicular to the wave fronts, $\lambda_{z,2D}$ has to be scaled by a factor $|\cos \Phi|$ given the approximation on the right hand side of (14). Figure 15 plots the maximum vertical MW wavelength calculated from UKMO analysis winds on this day using (14). The arrows show the wind velocities, which are directed nearly zonally. Figure 15 shows that northward of ∼40°S possible MWs have

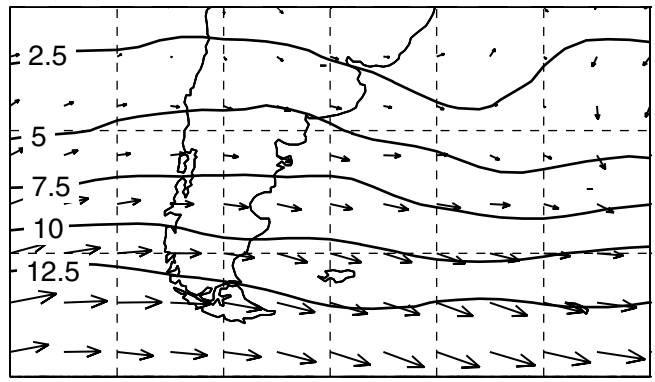


**Figure 15.** Contours of the upper limit of the vertical wavelength of MWs (labels in kilometers) on 6 November 1994 at 30 hPa. The values are calculated from UKMO winds and CRISTA background temperatures for the region from 30°S–60°S and 30°W–90°W. Overplotted are wind vectors indicating the wind direction and wind speed. Highest wind speeds shown (largest arrows) are 60 m $s^{-1}$.

vertical wavelengths too short to be detected by CRISTA (see Figure 6).

[60] Enhanced GW activity is observed in the lee of the Andes and above the Falkland Islands. However, the vertical wavelengths observed there are ∼20 km and therefore a factor ∼2 larger than (14) predicts. This indicates that the source of the observed waves is probably nonorographic. The observation of nonorographic waves near an isolated island on the southern hemisphere suggests parallels to the work of *Guest et al.* [2000], who described wave generation by a frontal system at the upwind side of Macquarie Island (55°S).

[61] The strongest GW amplitudes are observed at around 43°S. There are three consecutive profiles with high amplitudes and alternating phase. These three profiles have been discussed in detail by *Eckermann and Preusse* [1999]. They observed coherent wave oscillations at altitudes between 15 km and 30 km and inferred that these waves encountered a critical level at ∼43 km and break strongly at altitudes just below. The vertical wavelength as well as the amplitude growth with altitude provided strong evidence that these waves are MWs. A monochromatic sinusoidal wave can be expressed as [*Preusse et al.*, 2001b]

$$T'(x,z,t) = \hat{T}(z)\sin(kx + mz - \omega t + \phi) \qquad (15)$$

where $T'$ is the residual temperature, $\hat{T}$ denotes the temperature amplitude, $k = 2\pi/\lambda_x$ is the horizontal wave number, $m = 2\pi/\lambda_z$ is the vertical wave number, and $\omega = 2\pi/\tau$ is the ground-based frequency. For an observer at the ground $\omega = 0$ in the case of a MW. A phase variation in the vertical between two profiles sampling the same wave therefore indicates the same phase variation in the horizontal. This is also discussed by *Eckermann and Preusse* [1999] and *Preusse et al.* [2001b] in some detail. Thus, from Figure 14b one can conclude that the horizontal wavelength along the orbit track is either $\lambda_x$ = 400 km, in which case the phase changes by 180° between the subsequent profiles, or $\lambda_x$ = 130 km, in which case the

phase changes by 540° between the subsequent profiles. The latter would mean that CRISTA undersamples the wave and it seems that the question of whether $\lambda_x$ = 130 km or 400 km cannot be answered on basis of these CRISTA data alone.

[62] However, this question is directly related to the sensitivity discussion of section 2. At this location the main ridge of the Andes follows the coast line and the wind direction is nearly perpendicular to the ridge at all altitudes [*Tan and Eckermann*, 2000]. We therefore can assume that the wave crests are aligned with the coast line as well. This assumption is supported by the measured vertical wavelength, which is in excellent agreement with the two-dimensional dispersion relation (14) [*Eckermann and Preusse*, 1999] and therefore indicates a two-dimensional geometry. From Figure 14a we see that the three profiles with the high amplitudes are measured at an angle of about 45° between the line of sight and the coast line and hence the wave crests. Only a few kilometers apart are measurements from a second orbit where the line of sight was nearly perpendicular to the mountain ridge. From Figure 14b we see that the amplitudes measured during this orbit are vanishing (<1 *K*). The two sets of measurements were taken at 0624 GMT and 0453 GMT respectively. Using the same approximations as for (14) the vertical group velocity of a GW is given by [e.g., *Andrews et al.*, 1987]

$$c_{gz} = \frac{Nk}{m^2}, \tag{16}$$

and is $\sim$1 km h$^{-1}$ for a wave of 400 km horizontal and 6 km vertical wavelength. Thus, we do not expect the wave field to alter sufficiently during this short time difference between the two measurements to explain these large differences in the observed amplitudes. Thus we can only explain the different measured amplitudes if the horizontal wavelength is just at the edge of the sensitivity distribution described in Figure 6. This is the case if we assume a horizontal wavelength of 130 km, which is not visible to CRISTA if viewed perpendicular to the wave crests, but becomes visible when the wavelength along the line of sight is elongated to more than 200 km by viewing the wave crests at a significant angle $\alpha$ (see section 2.5 and Figure 9). This interpretation is further supported by investigations with a two-dimensional high resolution model [*Tan and Eckermann*, 2000].

[63] Figures 14c and 14d show the MM5 temperature field in the outer domain at 30 hPa at 0600 GMT on 6 November 1994 from two different simulations: Figure 14c without, Figure 14d with a local grid refinement. The three red points give the locations of the profiles investigated by *Eckermann and Preusse* [1999]. Only the higher resolution simulation exhibits significant stratospheric GW activity above these three points. Viewed optimistically, Profiles 1 and 2 are each located in Figure 14d at the eastern edge of a cold trough, indicated by deep blue, thus separated by about one wavelength. Profiles 2 and 3 are separated by a third cold trough and seem to be separated by one and a half wavelengths. For this interpretation one has to assume that the splitting of the large blue shaded trough spanning from 70°W, 40°S to 60°W, 50°S results in separate troughs. If we do so, the phase fronts are aligned parallel to the coast lines and waves

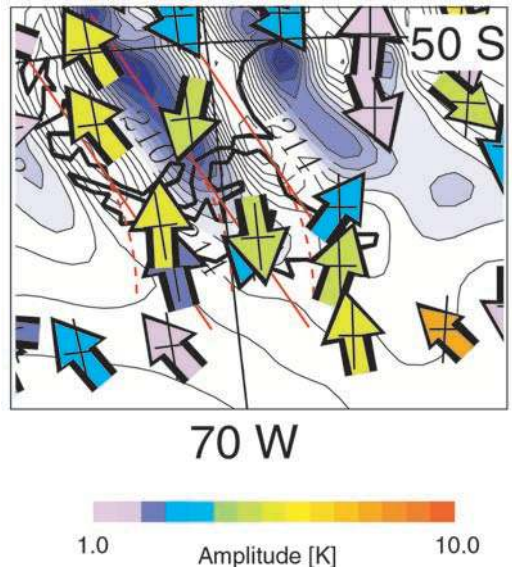


**Figure 16.** Enlargement of the region in the vicinity of Tierra del Fuego. Amplitude and phase information (cf. Figure 14b) are overplotted on MM5 high-resolution data (cf. Figure 14d). To guide the eye, MM5 phase fronts are extended to the south (red lines). The phases of the CRISTA profiles indicate that these turn southward toward a longitudinal direction on the south coast (red dashed lines).

detectable by CRISTA emerge. A wave front following the main direction of the large-scale trough results in too short a vertical wavelength and is not compatible with the CRISTA observations. Thus the MM5 model indicates a short horizontal wavelength of $\approx$130 km, too. However, the amplitudes in the MM5 results seem to be strongest in the vicinity of the main mountain ridge (westward of 70°W) and decreasing amplitudes are observed at the east coast (profile 3). This is much less pronounced in two-dimensional model simulations [*Tan and Eckermann*, 2000] and not found in the CRISTA measurements of the three profiles. Probably the model resolution will have to be further increased for this region. This, however, requires a higher resolution topographic data set within the MM5 model than the one which was available to the authors.

[64] The question of whether the wavelength of the GW observed near 42°S is more likely to be 130 km rather than 400 km is not purely academic. As has been pointed out by *Eckermann and Preusse* [1999], this single wave event carries a large part of the total momentum flux for this latitude and a 130 km wavelength wave would lead to three times larger momentum flux deposition (for a given temperature amplitude) than a 400 km wave.

[65] Good agreement between CRISTA data and the MM5 results is found at the southernmost tip of South America. The CRISTA data in Figure 14b show large amplitudes in the vicinity of Tierra del Fuego, reaching down to the southernmost boundary of measurements at 57°S. An enlarged map of this region is shown in Figure 16. The CRISTA profiles are overplotted on the high-resolution MM5 temperature field. In the CRISTA data we observe a phase front along the west coast with phases around 0°

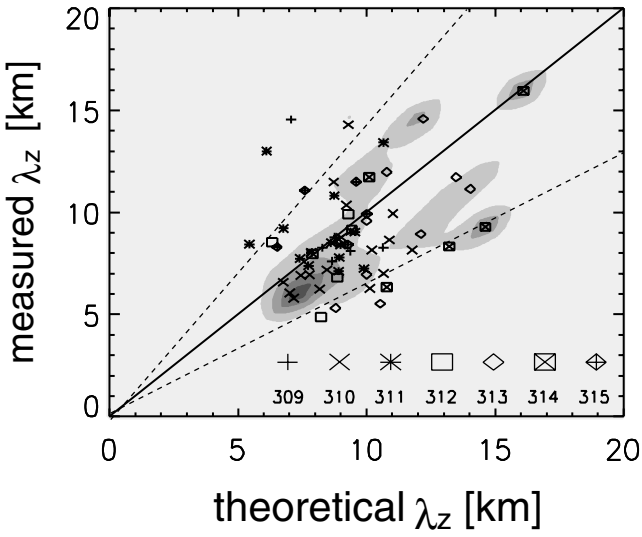


**Figure 17.** Scatterplot of measured versus theoretical vertical wavelength in the area 42°S–50°S. Symbols show data from different days, from day 309 (5 November) to day 315 (11 November). Almost all the data points lie within the error bars (dashed lines). The shading indicates amplitude-weighted point density. For details, see text.

(three northward-pointing arrows), a second one 200 km to the east with phases around 180° (three southward-pointing arrows) and a third front again 200 km further to the east at about 0°. (Note that at 55°S two profiles in the first and second phase front are overplotted on top of two other profiles with nearly the same orientation and a similar amplitude, respectively.) The profile at ~50°S, 73°W is not consistent with a stationary MW as the long vertical wavelength $\lambda_z > 20$ km indicates.

[66] A very similar structure is visible in the MM5 results. We find a cold trough eastward of the coast followed by warm and cold phases separated by ~200 km. The horizontal wavelengths retrieved from the measurement and the model are in good agreement. To make comparison easier the three red lines show the extension of the MM5 phase fronts to the south.

[67] The three CRISTA profiles at ~67°W are aligned nearly meridionally with even a slight tilt to the north east direction. The phase fronts produced by the MM5, however, are aligned approximately parallel to the coast line. Thus, if the southernmost profile is located just between trough and crest the northern profile is located in the trough. The phases observed by CRISTA show this behavior. The phases change from zero (southernmost profile) to a negative value (northern profile, slightly eastward direction). Thus, the comparison of the CRISTA and the MM5 data shows that the model agrees with the data in the horizontal wavelength (~400 km) and in the direction of the phase fronts. The amplitudes measured by CRISTA in this region are about 4–5 K. This compares very well with peak-to-peak variations of ~10 K in the MM5 results. The only difference is that the CRISTA measurements indicate wave trains propagating long distances downstream (eastward) over the open ocean down to 57°S, which is less pronounced in the MM5 model results. It further appears that at the south coast of Tierra del Fuego the phase fronts of the measured waves turn toward a longitudinal direction (see the red dashed line in Panel 6, cf. the phase direction of the three profiles on the west coast).

[68] From Figure 14a we see that the vertical wavelength of the waves at 55°S is about 10 km. The wind speeds shown in Figure 15 are directed slightly southeastward and thus blow at an angle $\Phi \approx 40°$ to the wave fronts at 55°S. We therefore expect the measured wavelength to be a factor of $\cos(40°) \approx 0.77$ shorter than the wavelength predicted in Figure 15, which indeed we find.

[69] *Eckermann and Preusse* [1999] evaluated the vertical wavelength on a statistical basis for the region northward of 50°S. We reproduce this diagram in Figure 17. The measured vertical wavelength is plotted versus the predicted upper limit wavelength using (14). Only wavelength estimates for oscillations with amplitudes larger than 2 K are shown. The shading gives the amplitude-weighted point density. The uncertainty of the retrieved vertical wavelength is taken from the scatter in Figure 5 (section 2) and is plotted with dashed lines. Only a very few points lie outside this error boundary. Note also the high point density at ~8 km vertical wavelength along the 1:1 line. This agreement between theoretical and observed wavelengths is evidence that the waves here are stationary MWs and furthermore that the wave fronts here are aligned approximately perpendicular to the wind vector.

[70] Data southward of 50°S are plotted in Figure 18. Here, as discussed above, we do not expect the values to be distributed tightly around the 1:1 line due to the nonzero $\Phi$ for waves here. We therefore draw the solid line $\lambda_{z,measured} = 0.77\lambda_{z,2D}$ onto Figure 18. As expected we find the majority of the waves now centered around the solid line and inside the respective error lines (dashed), indicative of $\Phi \sim 40°$.

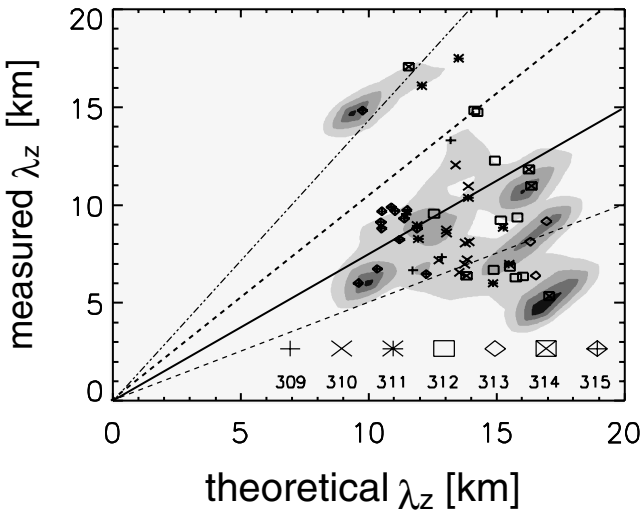


**Figure 18.** As for Figure 17, but for 50°S–57°S. The solid line indicates the expectations for wave fronts at an angle $\Phi = 40°$ to the mean background wind. Most points cluster around the solid line inside the error limits (dashed lines). The dashed-dotted line indicates $\lambda_{z,2D}$ plus the estimated precision uncertainty of CRISTA. For details, see text.

However, some waves may stem from singular mountains and should in this case have shorter wavelengths than the dashed-dotted line. Nonetheless, these wavelength estimates are entirely consistent with the tilted wave fronts simulated by MM5 (Figures 14c, 14d, and 16).

### 4.2. Interpretation Employing the GROGRAT Model

#### 4.2.1. Questions

[71] The close comparisons between CRISTA and MM5 data in Figures 14 and 16 show conclusively that CRISTA accurately measured and characterized stratospheric MWs over the Andes on 6 November 1994. To gain some physical insights into the MWs in both the CRISTA data and MM5 model results, we conducted detailed ray-tracing simulations. In particular, we wanted to answer the following questions.

[72] (1) Why do MWs with a horizontal wavelength ~130 km appear to dominate at 40–45°S, rather than the longer ~400 km wavelength noted further to the south? The Andean ridge remains quite wide here and might be expected to force a longer wave mode throughout [e.g., *Tan and Eckermann*, 2000]. Nonetheless, it does not arise here in either the data [see also *Eckermann and Preusse*, 1999] or MM5 results. Exactly why is unclear.

[73] (2) Why does a ~400 km horizontal wavelength wave dominate at ~50–55°S, and why does it have a noticeable northwest–southeast alignment of its phase lines (Figures 14 and 16)? Two possible explanations come to mind. First, the topography here "hooks," from north–south alignment to a more northwest–southeast aligned coastline at the southernmost tip of South America (e.g., Figure 14 of this paper and Plate 1 of *Tan and Eckermann*, [2000]). This might be expected to force a plane MW with northwest–southeast aligned phase fronts, which then propagates directly into the stratosphere.

[74] In addition, however, Figure 15 shows that there is strong latitudinal shear in the stratospheric zonal winds ($\partial U/\partial y$) over this region. The ray-tracing equation [*Dunkerton*, 1984; *Marks and Eckermann*, 1995]

$$\frac{dl}{dt} = -k\frac{\partial U}{\partial y}, \tag{17}$$

reveals that, for an initially westward wave vector ($k < 0$, $l = 0$), the strong latitudinal wind shear ($\partial U/\partial y < 0$) at 50–55°S in Figure 15 can lead to the development of a southward wave number component ($l < 0$) through lateral refraction. This yields a southwestward wave number vector ($k < 0$, $l < 0$) and thus northwest–southeast GW phase lines orthogonal to this wave vector, as observed in Figures 14 and 16. Ray-tracing simulations allow us to test both mechanisms to some extent.

[75] (3) Why do the longer MWs at ~45–55°S appear to propagate significant distances downstream of the Andes? One possible reason is that these longer wavelength waves (small $k$) are of inertia gravity waveform, such that $|kU/f| \sim O(1)$. Such low frequency MWs can leak downstream in two and three dimensions due to a mismatch between their horizontal phase and group velocities induced by Coriolis effects [e.g., *Dudhia*, 1993]. In three dimensions, however, even hydrostatic stationary MWs aligned at an angle to the mean flow can propagate downstream [e.g., *Smith*, 1980]. Transience, nonhydrostatic effects or nonlinearity can also yield downstream penetration of wave energy. Ray-tracing can be used to test the significance of inertial modifications and three-dimensionality to downstream penetration of wave energy here.

#### 4.2.2. Experiments

[76] Ray-tracing was performed with the Gravity Wave Regional or Global Ray Tracer (GROGRAT) Model [*Marks and Eckermann*, 1995; *Eckermann and Marks*, 1997]. The GROGRAT simulations reported here included refraction due to atmospheric gradients in all three spatial directions, but did not include time dependence of the background atmosphere. Wave amplitudes were solved using constancy of vertical wave action flux, and dissipation due to infrared damping, turbulent damping and saturation were all included: see the work of *Marks and Eckermann* [1995] for more details. The ray-tracing was performed through background atmospheres provided by analyses from NASA's Data Assimilation Office (DAO) [*Coy and Swinbank*, 1997] and the National Centers for Environmental Prediction (NCEP) reanalyses [*Kalnay et al.*, 1996; *Kistler et al.*, 2001]. NCEP and DAO ray-tracing results were broadly similar: we present the DAO-based results here due to their more complete stratosphere and some questions about the reliability of NCEP stratospheric data over the Andes [*Trenberth and Stepaniak*, 2002]. Results from 4 DAO ray-tracing experiments for 6 November 1994 at 0000 GMT are shown in Figure 19. These experiments were devised to cast light on the questions posed above.

[77] In all 4 cases, stationary MWs were launched from locations shown with green diamonds in Figure 19 at an altitude of 2 km (i.e., over and just above the Andes) with a starting horizontal velocity amplitude of 1 m $s^{-1}$. Note that no attempt was made here to assign different amplitudes based on the underlying topography, in contrast to MM5 results and the MW model simulations of *Eckermann and Preusse* [1999]. Waves were traced to an altitude of 24 km, which is ~30 hPa. Final amplitudes at 24 km in Figure 19 are given in terms of the normalized temperature perturbation, for easier comparisons with Figures 14 and 16. We traced two types of waves, one with an initial horizontal wavelength of 130 km, the other with a 400 km wavelength, results for which are shown in the left and right columns of Figure 19, respectively. In both cases we also launched the waves with two different azimuth groupings. In the first case, wave vectors were initially aligned westward $(\phi)_{init} = 0°$. These results are shown in the top row of Figure 19, and allow us to assess the role of latitudinal refraction in setting observed phase-tilts in the wave patterns. In the second case, southwestward wave vectors were imposed on the waves at their launch heights ($(\phi)_{init} = 20°$ and 40°), to mimic MWs launched by two-dimensional topography with a similar tilted alignment. Results for these waves are given in the bottom row of Figure 19. In all cases, waves with vertical wavelengths <5 km at the final height of 24 km were removed, to account for the insensitivity of CRISTA to these small vertical scales.

#### 4.2.3. Results

[78] The ray-tracing results in Figure 19 show several features that resemble both the CRISTA data and MM5 model results from Figures 14 and 16.

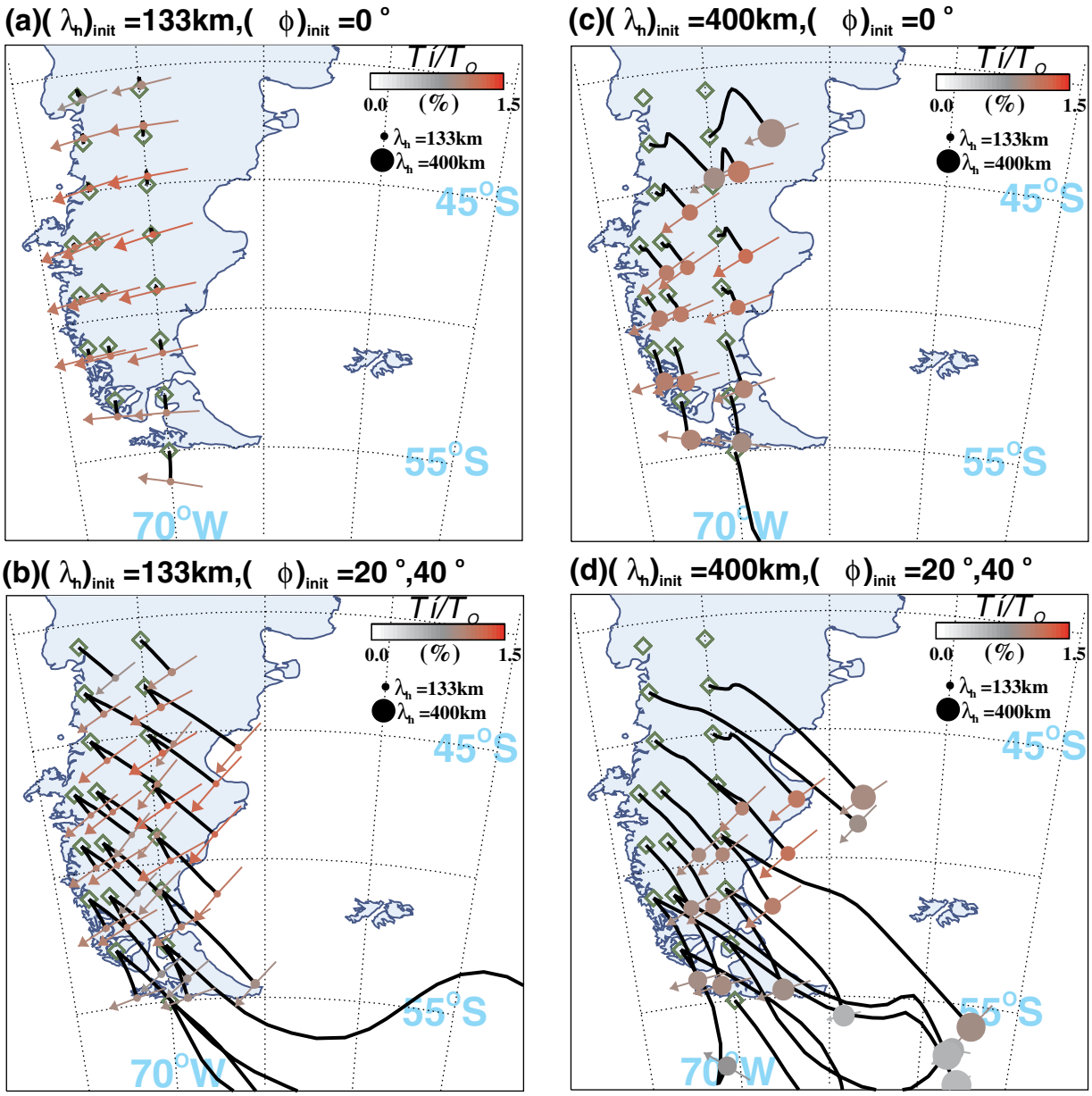


**Figure 19.** GROGRAT simulations of stationary MW propagation from 2 to 24 km using DAO "MAESAE" assimilations for 6 November 1994 at 0000 GMT. See text for further details on these simulations. Green diamonds show starting locations at 2 km. Thick black curves show the group propagation paths of those waves that propagate to 24 km and have vertical wavelengths ≥5 km. Vectors show wave number direction $\vec{K}_h = (k, l)$ at 24 km, with length equal to total normalized peak temperature amplitude (see also color code and color bar). Diameters of filled circles are proportional to the final horizontal wavelength $\lambda_h$ at 24 km. Results are shown for MWs of (a) initial horizontal wavelength $(\lambda_h)_{init}$ = 133 km and initial zonal (westward) wave number direction $\phi_{init} = 0°$, (b) $(\lambda_h)_{init}$ = 133 km and $\phi_{init} = 20°$ and 40° (southwestward), (c) $(\lambda_h)_{init}$ = 400 km and $\phi_{init} = 0°$, and (d) $(\lambda_h)_{init}$ = 400 km and $\phi_{init} = 20°$ and 40°.

[79] First, Figure 19a shows that a 130 km wavelength MW can reach the stratosphere at 40–43°S, whereas 400 km MWs initially aligned either westward (Figure 19c) or southwestward (Figure 19d) do not reach the stratosphere at ~40–43°S. This occurs in the GROGRAT simulations because low-level winds were sufficiently weak that wave frequencies near the ground were less than the local inertial frequency $|f|$: i.e., $|kU| < |f|$ for the 400 km waves. The 130 km waves, however, could propagate, since their larger $k$ values satisfied $|kU| > |f|$. This explains why a 400 km wave did not emerge in the stratosphere at these latitudes, despite the presence of very wide mountain ridges at ~40–50°S that could plausibly force such a wave.

[80] Figure 19a also shows that ray paths of the 130 km westward-aligned MWs barely deviate from their initial positions: i.e., they propagate almost purely vertically. This

indicates that the waves are hydrostatic and not affected by either rotational effects or three-dimensionality to any great degree (note that imposition of three-dimensionality via wave number tilts in Figure 19b did yield some downstream penetration, as expected [e.g., *Smith*, 1980]). Conversely, the 400 km westward-aligned wave groups in Figure 19c did propagate significant distances to the south and east. This is due to two effects. The first is inertial modification due to intrinsic frequencies that are not large compared to $|f|$. Second, a southward drift occurs due to development of meridional wave number components $l$ due to lateral refraction via (17), as can be seen from the tilted final wave number vector directions plotted in Figure 19c.

[81] While the tilts acquired due to refraction in Figure 19c are significant, they are not as large as those seen at 50–55°S in the MM5 results of Figures 14 and 16. Thus, some initial tilting due to curving topography here also appears to be needed. Figure 19d shows results for the 400 km waves with initial tilts of 20° and 40° imposed. The results here most closely resemble the MM5 results and CRISTA data at 50–55°S in Figures 14 and 16, in that this long-wavelength wave energy is confined mostly to latitudes ~50–55°S, has significant meridional wave numbers (and hence phase tilts), and exhibits greater penetration downstream of the Andes. Interestingly, it produces a region of very significant downstream penetration at ~52–55°S that resembles that seen in the CRISTA and MM5 data (Figures 14 and 16). Furthermore the waves at the south coast of Tierra del Fuego in Figure 19d have a much smaller meridional tilt than the waves slightly northward. Tierra del Fuego is already inside the polar vortex and so the latitudinal gradient of the zonal wind is much smaller or even reversed (cf. Figure 15). This meridional alignment is in agreement with the CRISTA results, where we found some indication for a turn to meridional alignment (Figure 16, red dashed lines).

[82] In summary, then, these GROGRAT simulations reveal that shorter wavelength waves at 40–45°S occur because 400 km waves cannot propagate from the Andes at these latitudes due to weak low-level winds, whereas shorter 130 km waves can propagate into the stratosphere. Further south, where winds are stronger throughout, the 400 km wave can propagate from topography and emerge strongly in the stratosphere, as observed. Its tilted phase alignment and strong downstream propagation appears to result mainly from the curved topography in this southernmost region of South America, but it is also accentuated by lateral refraction effects via (17) and inertial modifications.

## 5. Summary and Conclusions

[83] In the recent past a large number of GW observations from satellite instruments have been reported and upcoming missions will also search for GW signatures. However, so far the sensitivity to GWs has only been estimated in detail for instruments measuring saturated radiances [*Wu and Waters*, 1997; *McLandress et al.*, 2000]. In this paper a detailed estimation of the sensitivity to GWs of emission limb-sounding under optically thin conditions is presented. We have shown that one needs to consider the radiative transfer throughout a GW field in two dimensions. An analytical approximation derived in section 2.2 enabled us to separately discuss the limitations due to the radiative transfer, which are universal to all instruments using the same technique, and the limitations due to the sampling and retrieval, which are characteristic of the CRISTA instrument. In addition, numerical simulations based on a fast radiative transfer scheme [*Gordley et al.*, 1994; *Marshall et al.*, 1994] allow us to take into account variations of the background atmosphere as well as wave amplitude changes with altitude.

[84] Due to the radiative transfer, only waves with horizontal wavelengths longer than ~200 km along the limb ray can be detected. An unexpected decrease of sensitivity to short horizontal and long vertical wavelengths is found, which is very important for the intercomparison of recent GW climatologies obtained from different satellite instruments [*Alexander*, 1998; *Preusse et al.*, 2000]. The vertical sampling and the retrieval suppresses waves with vertical wavelengths shorter than about 5 km.

[85] The sensitivity varies only moderately with latitude and altitude. Thus, geographical distributions can be retrieved accurately from temperature data. We presented results of CRISTA's sensitivity to GWs using two numerical simulations: one with and one without amplitude growth dependent on altitude. Both runs agree well with each other and with the results from a simplified analytical approach. This indicates the basic generality of the obtained sensitivity estimates, which allows us to apply these results to other infrared limb scanning instruments. Two examples are LIMS [*Fetzer*, 1990; *Fetzer and Gille*, 1994, 1996], which has been used for previous studies, and, in future, HIRDLS, which will provide a long time series of high spatial resolution data and which therefore ought to be very well suited for GW studies based on our results here. For these instruments section 2 of this paper presents the sensitivity estimations imperative for any satellite GW analyses.

[86] In addition, for horizontal wavelengths below ~1000 km, the sensitivity does not depend to any significant extent on the degree of amplitude growth with altitude. For these shorter horizontal wavelengths (~300–800 km) the sensitivity depends almost entirely on the vertical wavelength (Figure 6). This universal behavior of the sensitivity allows us to deduce a one-dimensional correction factor, which compensates for the sensitivity changes as a function of vertical wavelength [*Preusse et al.*, 2000]. However, the detection limits of ~200 km horizontal wavelength along the LOS and ~5 km vertical wavelength still remain and cannot, of course, be compensated for.

[87] GW signals were extracted from CRISTA temperatures with the help of a Kalman filter and were analyzed using a combination of MEM and HA. This MEM/HA method compares well with the results obtained from Fourier Transforms, but provides a better altitude resolution. Both methods show that a low altitude tropical maximum in GW variances is observed in short vertical-wavelength GWs only. As has been shown recently by *Preusse et al.* [2000], this finding explains differences in the patterns observed by different satellite instruments. In particular the CRISTA data for wavelengths shorter than $\lambda_z < 10$ km agree very well with results from GPS/MET [*Tsuda et al.*, 2000]. The fact that we observe the tropical maximum only

at short vertical wavelengths is probably due to a relatively higher occurrence of low frequency and long horizontal wavelength waves in the equatorial region [*Alexander et al.*, 2002].

[88] In addition, the MEM/HA analysis provides the vertical wavelength of monochromatic wave trains as a function of altitude. The precision of these retrieved vertical-wavelength determinations is estimated to be approximately 25% (see Figure 5). This allows us to compare the wavelength of measured waves with theoretical predictions.

[89] The high spatial resolution of the CRISTA measurements is utilized in a case study of MWs observed in the stratosphere over the southern tip of South America. At about 43°S three profiles with very high amplitudes were observed on 6 November 1994. With the help of the sensitivity arguments discussed earlier we find evidence that the observed signatures stem from a MW with a horizontal wavelength of ~130 km. This finding is supported by numerical modeling with a two-dimensional high-resolution mesoscale model [*Tan and Eckermann*, 2000] and, in addition, by simulations employing the GROGRAT ray-tracing model [*Marks and Eckermann*, 1995; *Eckermann and Marks*, 1997]. The observed vertical wavelengths are for all observations northward of 50°N in good agreement with the theoretical expectations for a two-dimensional geometry. The results emphasize that a detailed knowledge of the radiative transfer is necessary to fully understand the satellite observations.

[90] At the southernmost tip of South America we find a rich field of waves of ~400 km horizontal wavelength. Here, the wave crests and troughs are no longer oriented orthogonal to the wind field. Thus, the vertical wavelength is shorter than predicted in a two-dimensional geometry (cf. Figure 18). The CRISTA observations agree with the MM5 results in horizontal wavelength (~400 km), amplitude (~5 K) and the alignment of the wave fronts. Ray-tracing calculations with the GROGRAT model indicate that the orientation of the wave fronts at an angle of ~40° with respect to the background wind is predominantly due to the hooklike topography at the southernmost tip of South America, although latitudinal shear in zonal wind is also an important effect.

[91] The observed waves extend further to the south than in the MM5 simulations. Still the agreement between the MM5 results and the measurements is excellent and leaves little doubt that CRISTA is accurately measuring and characterizing mesoscale MWs in this region of the stratosphere. It should be noted that CRISTA passes this region on three subsequent orbits and so the wave was viewed at different viewing angles. The results from these different overpasses agree well with each other, showing that a horizontal wavelength of $\lambda_z$ = 400 km is well above the sensitivity limit as was inferred in our sensitivity study in section 2.

[92] The horizontal sampling on 6 November was 200 km along track and 600 km across track for a single pass of the satellite [*Riese et al.*, 1999]. In the geographic region of the case study the horizontal resolution was further increased, because this region was located at the southern turning point of the orbit track. Therefore, the same region was sampled during subsequent orbits. The case study demonstrates that this very high horizontal resolution of the measurements is essential for revealing the spatial structure of the waves. In particular, the information about the three-dimensional spatial structure provides valuable test cases for numerical models. The comparison of the CRISTA results with the MM5 simulations demonstrates that the model captures the salient features of the GW field when run at a high resolution. However, the case study also provides evidence that a 200 km sampling along track is still too coarse to fully resolve the horizontal wave structures detected by the triple telescope CRISTA instrument. The detailed investigations of small-scale structures by CRISTA in the case study was only possible due to sampling the south tip of South America in several subsequent overpasses and is therefore a result of using three telescopes simultaneously. Thus a case study like the one presented here is at its present stage possible only with the triple-telescope CRISTA instrument and will be restricted in the near future to those instruments providing data of very high spatial resolution, i.e., the HIRDLS instrument.

[93] **Acknowledgments.** We sincerely thank T. B. Marshall and L. L. Gordley for supporting us in the use of the BANDPAK radiance model. We thank M. Ern for the implementation of the Kalman filter and D. Offermann for helpful comments. We further thank G. Eidmann and M. Bittner for comments on spectral analysis. Finally, we want to thank two reviewers for their helpful comments. The CRISTA experiment is funded by the Bundesministerium fuer Bildung und Forschung (BMBF, Berlin) through Deutsches Zentrum fuer Luft- und Raumfahrt (DLR, Bonn). Stephen Eckermann and Dave Broutman acknowledge support for this research through the Office of Naval Research and by NASA through the Office of Earth Science's Atmospheric Chemistry Modeling and Analysis Program (grants L68786D and W19946) and Office of Space Science's Geospace Sciences Program (grant W19862).

## References

Alexander, M. J., Interpretations of observed climatological patterns in stratospheric gravity wave variance, *J. Geophys. Res.*, *103*, 8627–8640, 1998.

Alexander, M. J., T. Tsuda, and R. A. Vincent, On the latitudinal variations observed in gravity waves with short vertical wavelengths, *J. Atmos. Sci.*, *59*, 1394–1404, 2002.

Allen, S. J., and R. A. Vincent, Gravity wave activity in the lower atmosphere: Seasonal and latitudinal variations, *J. Geophys. Res.*, *100*, 1327–1350, 1995.

Andrews, D. J., J. R. Holton, and C. B. Leovy, Middle atmosphere dynamics, *Int. Geophys. Ser.*, 489 pp., Academic, San Diego, Calif., 1987.

Bailey, P. L., and J. C. Gille, Inversion of limb radiance measurements: An operational algorithm, *J. Geophys. Res.*, *91*, 2757–2774, 1986.

Barnett, J. J., P. Venters, and J. C. Gille, Direct measurement of geopotential height by the HIRDLS instrument, *Adv. Space Res.*, *22*, 1497–1500, 1998.

Bittner, M., D. Offermann, and H. U. Widdel, Nonlinear resonant interaction of atmospheric gravity waves derived from chaff-wind data: A case study, Proceedings 13th ESA Symposium on European Rocket and Balloon Programmes and Related Research, Öland, Sweden, 26–29 May 1997, ESA SP 397, pp. 489–494, 1997.

Boville, B. A., Middle atmosphere version of CCM2 (MACCM2): Annual cycle and interannual variability, *J. Geophys. Res.*, *100*, 9017–9039, 1995.

Brasseur, G., and S. Solomon, *Aeronomy of the Middle Atmosphere*, 452 pp., D. Reidel, Norwell, Mass., 1986.

Carslaw, K. S., H. Volkert, P. Haynes, N. R. P. Harris, N. Larsen, G. Amanatidis, and T. Peter, Overview of the European workshop on mesoscale processes in the stratosphere, in *Mesoscale Processes in the Stratosphere*, edited by K. S. Carslaw and G. T. Amanatidis, *Air Pollut. Res. Rep.,* 69, EUR 18912 EN, 1999a.

Carslaw, K. S., T. Peter, J. T. Bacmeister, and S. D. Eckermann, Widespread solid particle formation by mountain waves in the Arctic stratosphere, *J. Geophys. Res.*, *104*, 1827–1836, 1999b.

Cot, C., and J. Barat, Wave–turbulence interaction in the stratosphere: A case study, *J. Geophys. Res.*, *91*, 2749–2756, 1986.

Coy, L., and R. Swinbank, Characteristics of stratospheric winds and tem-

peratures produced by data assimilation, *J. Geophys. Res.*, *102*, 25,763–25,781, 1997.

Dewan, E. M., R. H. Picard, R. R. O'Neil, H. A. Gardiner, J. Gibson, J. D. Mill, E. Richards, M. Kendra, and W. O. Gallery, MSX satellite observations of thunderstorm-generated gravity waves in mid-wave infrared images of the upper stratosphere, *Geophys. Res. Lett.*, *25*, 939–942, 1998.

Dörnbrack, A., and M. Leutbecher, Relevance of mountain wave cooling for the formation of polar stratospheric clouds over Scandinavia: A 20 year climatology, *J. Geophys. Res.*, *106*, 1583–1593, 2001.

Dörnbrack, A., M. Leutbecher, H. Volkert, and M. Wirth, Mesoscale forecasts of stratospheric mountain waves, *Meteorol. Appl.*, *5*, 117–126, 1998.

Dörnbrack, A., M. Leutbecher, R. Kivi, and E. Kyrö, Mountain wave induced record low stratospheric temperatures above northern Scandinavia, *Tellus*, *51a*, 951–963, 1999.

Dörnbrack, A., M. Leutbecher, J. Reichardt, A. Behrendt, K. P. Müller, and G. Baumgarten, Relevance of mountain wave cooling for the formation of polar stratospheric clouds over Scandinavia: Mesoscale dynamics and observations for January 1997, *J. Geophys. Res.*, *106*, 1569–1581, 2001.

Dudhia, J., A non-hydrostatic version of the Penn State-NCAR Mesoscale Model: Validation tests and simulation of an Atlantic cyclone and cold front, *Mon. Weather Rev.*, *121*, 1493–1513, 1993.

Dunkerton, T. J., Inertia gravity waves in the stratosphere, *J. Atmos. Sci.*, *41*, 3396–3404, 1984.

Dunkerton, T. J., The role of gravity waves in the quasi-biennial oscillation, *J. Geophys. Res.*, *102*, 26,053–26,076, 1997.

Eckermann, S. D., and C. J. Marks, GROGRAT: A new model of the global propagation and dissipation of atmospheric gravity waves, *Adv. Space Res.*, *20*, 1253–1256, 1997.

Eckermann, S. D., and P. Preusse, Global measurements of stratospheric mountain waves from space, *Science*, *286*, 1534–1537, 1999.

Eckermann, S. D., I. Hirota, and W. K. Hocking, Gravity wave and equatorial wave morphology of the stratosphere derived from long-term rocket soundings, *Q. J. R. Meteorol. Soc.*, *121*, 146–186, 1995.

Ern, M., Interpolation asynoptischer Satellitendaten, Diploma thesis, WU D 93-35, Wuppertal Univ. (BUGW), 1993.

Fetzer, E., A global climatology of middle atmosphere inertio-gravity waves, Ph.D. thesis, 270 pp., State Univ. of Colo. at Boulder, 1990.

Fetzer, E. J., and J. C. Gille, Gravity wave variances in LIMS temperatures, part I, Variability and comparison with background winds, *J. Atmos. Sci.*, *51*, 2461–2483, 1994.

Fetzer, E. J., and J. C. Gille, Gravity wave variance in LIMS temperatures, part II, Comparison with the zonal-mean momentum balance, *J. Atmos. Sci.*, *53*, 398–410, 1996.

Fritts, D. C., Gravity wave saturation in the middle atmosphere: A review of theory and observations, *Rev. Geophys.*, *22*, 275–308, 1984.

Garcia, R. R., and S. Solomon, The effect of breaking gravity waves on the dynamics and chemical composition of the mesosphere and lower thermosphere, *J. Geophys. Res.*, *90*, 3850–3868, 1985.

Gordley, L. L., B. T. Marshall, and D. A. Chu, Linepak: Algorithms for modeling spectral transmittance and radiance, *J. Quant. Spectrosc. Radiat. Transfer*, *52*, 563–599, 1994.

Gradshteyn, I. S., and I. M. Ryzhik, *Table of Integrals, Series, and Products*, fifth edition, Academic, San Diego, Calif., 1994.

Grell, G. A., J. Dudhia, and D. R. Stauffer, A description of the fifth-generation Penn State/NCAR mesoscale model (MM5), *Tech. Note 398*, 121 pp., Natl. Cent. for Atmos. Res., Boulder, USA, 1994.

Grossmann, K. U., D. Offermann, O. Gusev, J. Oberheide, M. Riese, and R. Spang, The CRISTA 2 mission, *J. Geophys. Res.*, *107*, doi:10.1029/2001JD000667, in press, 2002.

Guest, F. M., M. J. Reeder, C. J. Marks, and D. J. Karoly, Inertia-gravity waves observed in the lower stratosphere over Macquarie Island, *J. Atmos. Sci.*, *57*, 737–752, 2000.

Jiang, J. H., and D. L. Wu, UARS MLS observations of gravity waves associated with the Arctic winter stratospheric vortex, *Geophys. Res. Lett.*, *28*, 527–530, 2001.

Kalnay, E., et al., The NCEP/NCAR 40-year reanalysis project, *Bull. Am. Meteorol. Soc.*, *77*, 437–471, 1996.

Kistler, R., et al., The NCEP/NCAR 50-year reanalysis: Monthly-means CD-ROM and documentation, *Bull. Am. Meteorol. Soc.*, *82*, 247–267, 2001.

Leutbecher, M., Die Ausbreitung orographisch angeregter Schwerewellen in die Stratosphäre, DLR-Forschungsbericht 98-17, ISSN 1434-8454, Ph.D. thesis, Ludwig-Maximilians-Universität München, 1998.

Lindzen, R. S., Turbulence and stress owing to gravity wave and tidal breakdown, *Geophys. Res. Lett.*, *86*, 9707–9714, 1981.

Manzini, E., and N. A. McFarlane, The effect of varying the source spectrum of a gravity wave parameterization in a middle atmosphere general circulation model, *J. Geophys. Res.*, *103*, 31,523–31,539, 1998.

Manzini, E., N. A. McFarlane, and C. McLandress, Impact of the Doppler spread parameterization on the simulation of the middle atmosphere circulation using the MA/ECHAM4 general circulation model, *Geophys. Res. Lett.*, *102*, 25,751–25,762, 1997.

Marks, C. J., and S. D. Eckermann, A three-dimensional nonhydrostatic ray-tracing model for gravity waves: Formulation and preliminary results for the middle atmosphere, *J. Atmos. Sci.*, *52*, 1959–1984, 1995.

Marshall, B. T., L. L. Gordley, and D. A. Chu, Bandpak: Algorithms for modeling broadband transmissions and radiance, *J. Quant. Spectrosc. Radiat. Transfer*, *52*, 581–599, 1994.

Mayr, H. G., J. G. Mengel, C. A. Reddy, K. L. Chan, and H. S. Porter, Variability of the equatorial oscillations induced by gravity wave filtering, *Geophys. Res. Lett.*, *25*, 2629–2632, 1998.

McLandress, C., On the importance of gravity waves in the middle atmosphere and their parameterization in general circulation models, *J. Atmos. Terr. Phys.*, *60*, 1357–1383, 1998.

McLandress, C., M. J. Alexander, and D. L. Wu, Microwave Limb Sounder observations of gravity waves in the stratosphere: A climatology and interpretation, *J. Geophys. Res.*, *105*, 11,947–11,967, 2000.

Mertens, C. J., M. G. Mlynczak, M. Lopez-Puertas, P. P. Wintersteiner, R. H. Picard, J. R. Winick, L. L. Gordley, and J. M. Russel III, Retrieval of mesospheric and lower thermospheric kinetic temperature from measurements of $CO_2$ 15μm Earth limb emission under non-LTE conditions, *Geophys. Res. Lett.*, *28*, 1391–1394, 2001.

Nastrom, G. D., and D. C. Fritts, Sources of mesoscale variability of gravity waves, part I, Topographic excitation, *J. Atmos. Sci.*, *49*, 101–110, 1992.

Nastrom, G. D., A. R. Hansen, T. Tsuda, M. Nishida, and R. Ware, A comparison of gravity wave energy observed by VHF radar and GPS/MET over central North America, *J. Geophys. Res.*, *105*, 4685–4687, 2000.

Oberheide, J., M. E. Hagan, W. E. Ward, M. Riese, and D. Offermann, Modeling the diurnal tide for CRISTA 1 time period, *Geophys. Res. Lett.*, *105*, 24,917–24,929, 2000.

Offermann, D., K. U. Grossmann, P. Barthol, P. Knieling, M. Riese, and R. Trant, The CRyogenic Infrared Spectrometers and Telescopes for the Atmosphere (CRISTA) experiment and middle atmosphere variability, *J. Geophys. Res.*, *104*, 16,311–16,325, 1999.

Picard, R. H., R. R. O'Neil, H. A. Gardiner, J. Gibson, J. R. Winick, W. O. Gallery, A. T. Stair, P. P. Wintersteiner, E. R. Hegblom, and E. Richards, Remote sensing of discrete stratospheric gravity-wave structure at 4.3-μm from the MSX satellite, *Geophys. Res. Lett.*, *25*, 2809–2812, 1998.

Press, W. H., S. A. Teukolsky, W. T. Vetterling, and B. P. Flannery, *Numerical Recipes in Fortran 77: The Art of Scientific Computing*, 2nd edition, 933 pp., Cambridge Univ. Press, New York, 1992.

Preusse, P., B. Schaeler, J. Bacmeister, and D. Offermann, Evidence for gravity waves in CRISTA temperatures, *Adv. Space Res.*, *24*, 1601–1604, 1999.

Preusse, P., S. D. Eckermann, and D. Offermann, Comparison of global distributions of zonal-mean gravity wave variance inferred from different satellite measurements, *Geophys. Res. Lett.*, *27*, 3877–3880, 2000.

Preusse, P., S. D. Eckermann, J. Oberheide, M. E. Hagan, and D. Offermann, Modulation of gravity waves by tides as seen in CRISTA temperatures, *Adv. Space Res.*, *27*, 1773–1778, 2001a.

Preusse, P., G. Eidmann, S. D. Eckermann, B. Schaeler, R. Spang, and D. Offermann, Indication of convectively generated gravity waves in CRISTA temperatures, *Adv. Space Res.*, *27*, 1653–1658, 2001b.

Queney, P., The problem of airflow over mountains: A summary of theoretical studies, *Bull. Am. Meteorol. Soc.*, *29*, 16–27, 1948.

Riese, M., Das CRISTA-Me system: Struktur und Anwendungen, Dissertation WUB-DIS 94-3, Wuppertal Univ. (BUGW), 1994.

Riese, M., R. Spang, P. Preusse, M. Ern, M. Jarisch, D. Offermann, and K. U. Grossmann, CRISTA data processing and atmospheric temperature and trace gas retrieval, *J. Geophys. Res.*, *104*, 16,349–16,367, 1999.

Riggin, D., D. C. Fritts, C. D. Fawcett, and E. Kudeki, Observations of inertia-gravity wave motions in the stratosphere over Jicamarca, Peru, *Geophys. Res. Lett.*, *22*, 3239–3242, 1995.

Roche, A. E., J. B. Kumer, J. L. Mergenthaler, G. A. Ely, W. G. Uplinger, J. F. Potter, T. C. James, and L. W. Sterrit, The Cryogenic Limb Array Etalon Spectrometer (CLAES) on UARS: Experiment description and performance, *J. Geophys. Res.*, *98*, 10,763–10,775, 1993.

Rodgers, C. D., Statistical principles of inversion theory, in *Inversion Methods in Atmospheric Remote Sounding*, edited by A. Deepak, Academic, San Diego, Calif., 1977.

Schoeberl, M. R., The penetration of mountain waves into the middle atmosphere, *J. Atmos. Sci.*, *42*, 2856–2864, 1985.

Sica, R. J., and A. T. Russell, How many waves are in the gravity wave spectrum?, *Geophys. Res. Lett.*, *26*, 3617–3620, 1999.

Smith, R. B., Linear theory of stratified hydrostatic flow past an isolated mountain, *Tellus*, *32*, 348–364, 1980.

Summers, M. E., D. E. Siskind, J. T. Bacmeister, R. R. Conway, S. E.

Zasadil, and D. F. Strobel, Seasonal variation of middle atmospheric CH4 and H2O with a new chemical-dynamical model, *J. Geophys. Res.*, *102*, 3502–3526, 1997.

Tan, K. A., and S. D. Eckermann, Numerical simulations of mountain waves in the middle atmosphere over the southern Andes, in *Atmospheric Science Across the Stratopause*, Geophysical Monograph 123, edited by D. E. Siskind et al., Am. Geophys. Union, Washington, D. C., 2000.

Trenberth K. E., and D. P. Stepaniak, A pathological problem with NCEP reanalyses in the stratosphere, *J. Clim.*, *15*, 690–695, 2002.

Tsuda, T., T. E. VanZandt, M. Mizumoto, S. Kato, and S. Fukao, Spectral analysis of temperature and Brunt-Väisälä frequency fluctuations observed by radiosondes, *J. Geophys. Res.*, *96*, 17,265–17,278, 1991.

Tsuda, T., M. Nishida, C. Rocken, and R. H. Ware, A global morphology of gravity wave activity in the stratosphere revealed by the GPS occultation data (GPS/MET), *J. Geophys. Res.*, *105*, 7257–7273, 2000.

Wang, D. Y., W. E. Ward, B. H. Solheim, and G. G. Shepherd, Wavenumber spectra of horizontal wind and temperature measured with WINDII, part I, Observational results, *J. Atmos. Sol.-Terr. Phys.*, *62*, 967–979, 2000a.

Wang, D. Y., W. E. Ward, B. H. Solheim, and G. G. Shepherd, Wavenumber spectra of horizontal wind and temperature measured with WINDII, part II, Diffusive effect on spectral formation, *J. Atmos. Sol.-Terr. Phys.*, *62*, 981–991, 2000b.

Wang, D. Y., W. E. Ward, Y. J. Rochon, and G. G. Shepherd, Airglow intensity variations induced by gravity waves, part 1, Generalization of the Hines–Tarasick's theory, *J. Atmos. Sol.-Terr. Phys.*, *63*, 35–46, 2001a.

Wang, D. Y., Y. J. Rochon, S. P. Zhang, W. E. Ward, R. H. Wiens, D. Y. Liang, W. A. Gault, and B. H. Solheim, Airglow intensity variations induced by gravity waves: Part 2, *J. Atmos. Sol.-Terr. Phys.*, *63*, 47–60, 2001b.

Ward, W. E., J. Oberheide, M. Riese, P. Preusse, and D. Offermann, Tidal signatures in temperature data from the CRISTA-1 mission, *J. Geophys. Res.*, *104*, 16,391–16,403, 1999.

Wu, D. L., and J. W. Waters, Gravity-wave-scale temperature fluctuations seen by the UARS MLS, *Geophys. Res. Lett.*, *23*, 3289–3292, 1996a.

Wu, D. L., and J. W. Waters, Satellite observations of atmospheric variances: A possible indication of gravity waves, *Geophys. Res. Lett.*, *23*, 3631–3634, 1996b.

Wu, D. L., and J. W. Waters, Observations of gravity waves with the UARS Microwave Lims Sounder, in *Gravity Wave Processes and Their Parameterization in Global Climate Models*, edited by K. Hamilton, Springer-Verlag, New York, 1997.

---

J. T. Bacmeister, Goddard Earth Sciences and Technology Center (GEST), University of Maryland, Baltimore County (UMBC) Baltimore, MD 21227-3898, USA. (bacmj@janus.gsfc.nasa.gov)

D. Broutman, Computational Physics, Inc., 8001 Braddock Road, Suite 210, Springfield, VA 22151, USA. (daveb@uap2.nrl.navy.mil)

A. Dörnbrack, Institut für Physik der Atmosphäre, Deutsches Zentrum für Luft und Raumfahrt (DLR), D-82230 Oberpfaffenhofen, Germany. (andreas.doernbrack@dlr.de)

S. D. Eckermann, E. O. Hulburt Center for Space Research, Code 7641.2, Naval Research Laboratory, Washington, DC 20375-5352, USA. (eckerman@uap2.nrl.navy.mil)

K. U. Grossmann and B. Schaeler, Department of Physics, Wuppertal University, Gauss Str. 20, D-42097 Wuppertal, Germany.

P. Preusse and M. Riese, ICG-I, Forschungszentrum Jülich, 52425 Jülich, Germany. (preusse@wpos2.physik.uni-wuppertal.de)